Nationaal Lucht- en Ruimtevaartlaboratorium
National Aerospace Laboratory NLR

NLR-TP-2000-487

Maturation of a full potential based rotor flow field code

M.H.L. Hounjet, J.C. Le Balleur, D. Blaise, G. Bernardini and A. Pisoni

Nationaal Lucht- en Ruimtevaartlaboratorium
National Aerospace Laboratory NLR

NLR-TP-2000-487

Maturation of a full potential based rotor flow field code

M.H.L. Hounjet, J.C. Le Balleur[1], D. Blaise[1], G. Bernardini[2] and A. Pisoni[3]

1. ONERA, France
2. Universita di Roma Tre, Italy
3. AGUSTA, Italy

This report is based on a presentation held at the 26th European Rotorcraft Forum, The Hague, The Netherlands on September 26-29, 2000.

Division:	Fluid Dynamics
Issued:	October 2000
Classification of title:	Unclassified

Summary

The paper presents the maturation of a full potential flow solver whose primitive form [1] was developed in the Brite-Euram project HELISHAPE, and aiming at a robust and fast aerodynamic system, ready for industrial applications.

In particular the modelling of blade boundary layers, the modelling of the vortex wake system, the inviscid potential flow solver methodology and the grid generator are described.

The resulting system is able to carry out the viscous non-linear aerodynamic analysis of rotorcraft blade configurations in realistic hover and forward flight conditions.

Calculated results are presented for 2D airfoils, 3D wings and isolated rotors.

Contents

(59 pages in total)

Symbol	Description
a	shape parameter
A	viscous function
c	correction associated with RHS
C_L	convergence characteristic $=\|\|\phi\|\|_{te}$
C_f	skin friction
C_p	pressure coefficient: $\frac{p - p_\infty}{\frac{1}{2}\rho_\infty q_{local}^2}$
C_T	thrust coefficient
c_{ref}	reference wing/blade airfoil chord
D	laminar damping function
F	damping function
k	reduced frequency: $k = \frac{\omega c_{ref}}{v_\infty}$
L	mesh level
M	Mach number
$M_{\omega R}$	rotational tip Mach number
N	number of mesh points
ni	number of computational cells in $chord$-wise direction
nj	number of computational cells in $span$-wise direction
nk	number of computational cells in $normal$-wise direction
p	pressure
q	inviscid velocity
q_{local}	local wing/rotor-blade element free stream velocity; $q_{local} = v_\infty$ wing; $q_{local} = \omega r + v_\infty \sin\Psi$ rotor
r	blade radius position
r	polar coordinate
R	residual
R	rotor radius
s_{le}	curvilinear absciss along the leading edge of the outer blade cut

continued on next page

continued from previous page

Symbol	Description
v_∞	free stream velocity
W	wake coefficient
x, y, z	Cartesian coordinates
xy	rotor disk plane
xz	symmetry plane
z	normal coordinate in boundary layer
α	angle of attack
$\bar{h}_t$	viscous enthalpy
$\bar{u}$	tangential component of viscous velocity.
β	$\frac{1}{M_{le}}$
δ	boundary layer thickness
δ^1	displacement thickness
η, η^*	viscous parameters
γ	ratio of specific heats
κ	Von Kármán constant: 0.41
μ	advance ratio in the direction of the x axis in the AF
ω	angular velocity of the rotor
Ψ	azimuthal angle
ρ	density
σ	rotor solidity
θ	pitch angle
φ	polar coordinate
h_t	inviscid enthalpy
Re_δ	the local Reynolds number based on ρq and δ.
$\|\|c\|\|_\infty$	convergence characteristic
$\|\|R.c\|\|_1$	convergence characteristic
c	local wing/blade airfoil chord
Re	Reynolds number
S	wing semi-span

continued on next page

continued from previous page

Symbol	Description
Indices	
^{n}	current time station, referring to $(n)^{th}$ timestep
$^{n+1}$	next time station, referring to $(n+1)^{th}$ timestep
Miscellaneous	
2D	two dimensional
3D	three dimensional
AF	absolute (inertial) frame of reference
AF	approximate factorization
AF3	approximate factorization
AGARD	Advisory Group for Aerospace Research and Development
ALPHAM	mean angle of attack
BEM_NEW	operational request parameter of HELIFPX with respect to number of fixed wake helicoidals
BEM	boundary element method
CFD	computational fluid dynamics
CFL	Courant-Friedrichs-Levy
CH	topology grid, C in xz plane, H in yz plane
CIRA	Centro Italiano Ricerche Aerospaziali S.C.p.A. (CIRA)
CONS	time-consistent solution procedure
CPU	central processing unit
DALPHA	amplitude of angle of attack
DERA	Defence Evaluation and Research Agency, United Kingdom
EROS	Brite-Euram III project: Development of a Common European Euler Code for Helicopter Rotors
EROS	Euler ROtorcraft Software
F-GMRES	matrix-free GMRES
F-GM	matrix-free GMRES
FAS-MG	full approximate storage multi-grid
GEROSV	chimera grid generation system including VIS12.GRID
GEROS	chimera grid generation system

continued on next page

continued from previous page

Symbol	Description
GMRES	generalized minimum residual algorithm
GNRTS	operational request parameter of HELIFPX with respect to number of time steps in a cycle
HELIFPX	enhanced aerodynamic prediction system dedicated to flow about rotor blades
HELIFP	full potential solver dedicated to flow about rotor blades
HELINOISE	Brite-Euram pilot phase project: Helicopter and Tiltrotor Aircraft Exterior Noise Research
HELISHAPE	Brite-Euram II project: Rotorcraft Aerodynamics and Aeroacoustics
IORDET	operational request parameter of HELIFPX with respect to temporal order of accuracy; IORDET $= 1$ first order temporal accuracy IORDET $= 2$ second order temporal accuracy
ITS	operational request parameter of HELIFPX with respect to update frequency of the non-linear boundary-layer
L-GMRES	AF3 preconditioned GMRES
L-GM	AF3 preconditioned GMRES
LHS	left hand side of system of equations
LTS	local time stepping
MDL	operational request parameter of HELIFPX with respect to turbulence model; MDL $= 0$ algebraic MDL $= 2$ two-equation "$k - u'v'$"
MGFS	operational request parameter of HELIFPX with respect to FAS-MG algorithm; MGFS $= 0$ application of FAS-MG MGFS $= 1$ full multi-grid application of FAS-MG
MYGMRS	operational request parameter of HELIFPX with respect to GMRES algorithm; MYGMRS $= 0$ application of linear GMRES with AF3 preconditioner MYGMRS $= 1$ application of matrix-free GMRES

continued on next page

continued from previous page

Symbol	Description
NLR	Stichting Nationaal Lucht- en Ruimtevaartlaboratorium (NLR)
NWITER	operational request parameter of HELIFPX with respect to number of subiterations
O1	First order temporal accuracy
O2	Second order temporal accuracy
ONERA	Office National d'Études et de Recherches Aérospatiales (ONERA), France
RANS	Reynolds averaged Navier Stokes
RBK	red-black ordered implicit line relaxation along k
RHS	right hand side of system of equations
ROSAA	Brite-Euram III project: Integration of Advanced Aerodynamics in Comprehensive Rotorcraft Analysis
RSHUB	operational request parameter of GEROSV with respect to chordwise spacing along hub
RSTIP	operational request parameter of GEROSV with respect to chordwise spacing along tip
TC-U4	HELISHAPE test case
TCV	time-consistent solution procedure
VII	viscous-inviscid interaction
VIS05	viscous correction system
VIS12.GRID	CH grid generator
V	V cycle strategy in multi-grid method

Subscripts and superscripts

∞	ambient (free stream) value
le	leading edge
$local$	local value
$incompressible$	incompressible value
$compressible$	compressible value
te	trailing edge

1 Introduction

In the development of modern rotorcraft, steady and unsteady aerodynamic analysis is required in a large design space to predict performance, acoustics, fatigue, vibrations, stability and control.

This implies a driving need for development of efficient computer methods to study the unsteady flow about realistic rotorcraft configurations

The flow field around the helicopter rotor is complex and also the dynamics of the rotating blades are not trivial. The adequate modelling of unsteady aerodynamics and the geometric state of the blades is a prerequisite to perform the aforementioned analysis.

Typically the rotor flies in its own wake of shed/trailed vorticity, and experiences very large rates of dynamic changes in geometry as well as flow (shock-induced separation, dynamic stall, shock waves). The problem poses specific requirements to aerodynamic solvers and grid generating procedures.

The HELIFP code and the VIS12.GRID developed in the Brite-Euram HELISHAPE project (1993-1996), concerning a full potential flow field solver and a CH topology type grid generator for the prediction of the flow about rotor blades, have partly addressed the industrial need of a dedicated system capable for performing routine CFD applications of high confidence coupled to comprehensive rotor codes.

To comply with industrial demands, the ROSAA consortium [1] has decided to continue the development of the aforementioned codes in order to develop a rotor aerodynamic prediction system able to efficiently predict aerodynamic quantities of interest.

This maturation process has resulted in the HELIFPX and the GEROSV codes which are part of the common integrated ROSAA system [2]. The latter is also loosely coupled to common rotor comprehensive methods [2] and acoustic methods, for the analysis of aerodynamics and acoustics of flexible rotorcraft and addresses the industrial need for a rotor aerodynamic prediction system able to efficiently predict aerodynamic quantities of interest (blade loads, blade torque etc) to the blade designer over a wide range of flight conditions, from hover to high-speed forward flight.

[1] The ROSAA consortium partners are Agusta,GKN-Westland, CIRA, DERA, NLR, ONERA and the University Rome III.

[2] To model the flow in the domains where the current model is not applicable (reversed flow, shock-induced separation, dynamic stall) and the elastic state of the geometry.

For the development of HELIFPX, existing HELIFP[1], VIS05[3] and EROS [4] formulations and code implementations have been used as a starting point.

The aerodynamic ”potential flow” solver of the rotor simulation system is based on a zonal approach in which the following 3 models are involved which are linked with *inflow* corrections at their computational borders:

- The outer flow about an isolated blade and its nearby wake system is modelled using a second order time-accurate fully-conservative finite-volume full-potential model fortified with an entropy correction model which further employs mass-flux splitting, Riemann invariant boundary conditions at far field, free stream consistency corrections, fixed wake with zero pressure jump and mass-flux, hard wall and transpiration wall boundary conditions, lumping terms to avoid odd-even coupling and consistent start of the Newton sub-iteration process. The spatial accurracy is first and second order for supersonic and subsonic flow, respectively. For a complete mathematical description of the model the reader is referred to [1]. The formulation of the solver is similar to the one as presented in [5]. The method requires a blade conforming CH topology grid. Transpiration boundary conditions are used to model non uniform free stream interactions: the effect of rotorcraft wake system and the other blades, the boundary layer and elastic deformation.
- The inner flow about an isolated blade and its nearby wake system is modelled with a viscous interaction model in which a hybrid field-integral boundary-layer method [6] is the building block. The separation capability of this field-integral boundary layer method has however been restricted to incipient separation. The physical model of the boundary layer method is based on the nonstationary first order boundary layer equations extended by the Le Balleur’s ”Defect Formulation” theory of viscous-inviscid interaction. This formulation allows the layer to be thick, and the normal pressure gradient to be non-zero but matched with the overlaying inviscid one. Second order ”corrections” on the normal pressure gradient provide a ”wake-curvature effect” (pressure jump prescribed to the inviscid flow along the wake-cut). The viscous-inviscid interaction belongs to the category of ”time-consistent” strong coupling. This means that at the end of a time step both the inviscid as well as the viscous model are converged.
- The balance of the flow field is modelled with a boundary element method based fixed and free wake modelling which allows for blade-vortex interaction studies and provides an adequate prediction of the wake-induced velocity field which has to be taken into account as a result of the finite computational domain used by the outer flow solver. The method allows for the prediction of pressure distributions on the blades based on an incompressible

and/or linear compressible potential model also. The physical model of the wake module is limited to those cases in which nonlinear transonic effects are negligible (*i.e.,* shock-free subsonic flows). The formulation is based on the assumption that the velocity field is potential (potential-flow model). This is true in the limited case of a inviscid, non-conducting, initially homentropic and initially irrotational flow.

Maturation of this flow solver system pertains to the following items at three levels (mathematical, numerical, implementational):

Mathematical :

m.1 Boundary element model for the prediction of pressure distributions on the blades and the wake-induced inflow based on an incompressible and/or linear compressible potential model.

m.2 Coupling full potential flow and the inflow of the boundary element model.

m.3 Two-dimensional laminar and turbulent boundary-layers to enhance physical realism for attached-separated flows and flows with strong shocks up to incipient separation.

m.4 Coupling boundary layer flow and full potential flow.

Numerical :

n.1 Second order temporal accuracy to enable forward flight simulation with larger time steps.

n.2 Three options to accelerate the iterative scheme solving the discretized full potential model:

- approximate factorization (AF3) [1, 5],
- Krylov accelerator of generalized minimum residuals (GMRES)[7] and
- full approximation storage multi-grid (FAS-MG) acceleration [8].

n.3 Options for compressible and incompressible wake analysis to provide an adequate prediction of the wake-induced velocity field.

Implementational :

i.1 A well structured I/O interface and user interface module which builds on a dedicated module which has been developed for the Euler code and the gridgenerator in the EROS project [4].

i.2 A communal Input and Output module which allows for easy coupling with other components of the rotor simulation system.

i.3 Options for boundary element method wake geometry modelling (helicoidal, Landgrebe or user specified, *e.g.*, from the free wake analysis model).

i.4 Options for inflow modelling (lifting line, lifting surface or far field) using the internal BEM inflow or user specified inflow.

i.5 Options for flow field database storage to enable postprocessing by the acoustic modules of the rotor system.

The grid generator of the rotor simulation method easily generates grids of CH topology and of high quality about helicopter blades as required by the flow solver code, and features:

g.1 The automatic special-purpose algebraic grid generator [1] for generating single-block standard grids of CH topology with high resolution and quality, both for periodic and non-periodic blades, extended with options to tailor the computational domain near the blade tip to enhance the accuracy of acoustic predictions and to accommodate complex tip shapes.

g.2 The grid generator system developed in the EROS project [9] with its structured I/O interface and user interface module and the visualization module.

In the following sections the discussion is restricted to the aerodynamics (items m.1, m.2, m.3, m.4, n.1, n.2, n.3) and the grid generation (item g.1). For a discussion of the other items the reader should consult [2, 10].

Finally the experience in verification to airfoils, fixed wings and rotorcraft configurations is presented.

2 Free-wake and far wake model

The description of the wake-induced velocity field is a prerequisite for obtaining adequate results with CFD methods which employ finite computational domains and/or are prone to wake dissipation.[1]

The accurate modelling of the wake-induced velocity field together with the accurate geometric state description of the blade is vital for the adequate prediction of the performance and forces acting on the helicopter.

It is well known that an accurate evaluation of the wake surface geometry is of fundamental importance here, especially for the case of rotors in hover and in forward flight at low advance ratio, in which the wake spirals are very close to the blade rotors and have a strong impact on the pressure distribution over the surface of the blades.

The prescribed wake modelling which is based on a boundary integral equation methodology (BEM) has been initially developed in the EROS project and is extended to free-wake modelling for elastically deformed blades. Coupling techniques have been developed between the BEM wake and the full potential code.[2]

Specifically, a boundary integral formulation for the velocity potential introduced in [11] for the analysis of potential flows around lifting rotors in compressible subsonic flow is utilized to generate the wake-inflow model with the following features:

- A time-accurate incompressible flow free wake formulation for an elastically deforming rotor blade having a complex tip geometry in forward flight.
- The stability of the free-wake algorithm is improved by the development of intermediate and far-wake models and by a proper choice of the vortex core (related, for instance, to the viscous wake thickness).
- Exact far field boundary conditions for the full potential code.

The coupling to the outer flow potential solver is performed by using two alternate approaches:

- inclusion of a transpiration velocity correction (predicted by BEM) in the computation of solid-wall boundary conditions.

[1] The prediction of pressure distributions on the blades based on an incompressible and/or linear compressible potential model is also provided

[2] It should be noted that the wake inflow might be obtained alternatively from external rotor codes or by builtin relatively simple theoretical models (momentum theory, blade element theory)

- evaluation of far-field boundary conditions by using values of flow variables at the external boundary of the computational domain predicted by BEM.

A distinguishing feature of the present wake-inflow model is that it includes a free-wake analysis. This means that the shape of the wake surface is unknown and follows from the flowfield solution by BEM. The geometry of the wake surface at each time step is modified by assuming that each wake point moves according to the induced-velocity field.

The following simplifications are performed in the free-wake model:

- The governing equation is assumed incompressible, which is an admissible approximation as experimental inspections have revealed.
- A limited number of wake spirals close to the blades is applied.
- A far-wake model is developed which deals with the remaining part [12]. The simulation of the far-wake effects is based on modelling the complex vortical structures in the far field with a few number of vortices collapsing in a single vortex that simulates the tip-vortex effects. The latter approach is motivated by the fact that in a rotor wake the effects due to the tip-vortex are much higher than those due to the vortex sheet, and therefore the aerodynamic effects induced by the isolated tip-vortex can be considered a satisfactory approximation of the effects of the entire far wake on the aerodynamic field.
  The model is obtained as a series of successive approximations:

  1. the far wake, is considered as fully rolled-up, *i.e.,* its effect is essentially that due to the tip vortex. In particular, the effects of the root vortex and of the *unsteady vorticity* (i.e., the vorticity in the radial direction, due to the unsteadiness of the sectional load distribution) are neglected,
  2. the tip-vortex spirals are assumed to be closely spaced so that the tip vortex is replaced with a continuous vorticity distribution, and
  3. the surface vortical distribution is replaced by an equivalent disk of sources and doublets placed in the wake cut-off plane.

- A intermediate wake-model is developed in order to minimize the numerical instabilities. The velocity field is computed a priori from the wake model by Landgrebe (see, *e.g.,* [13] and [14] for hovering rotors and that by Egolf and Landgrebe [15] for advancing rotors). Note that the geometry of the intermediate wake is updated at each time step, but the velocity field is evaluated initially and never updated. The inclusion of the intermediate-wake model assures that the wake spirals are moved uniformly and the geometry of the wake remains smooth, even in the region close to the far-wake disk.

- Finally, an approximated vortex-core model is embedded. In order to improve the robustness of the algorithm, it is assumed that the vortex filaments have a finite core (artificial viscosity).

3 Viscous model

Viscous modelling aims at improving blade loads and moments predictions, and thus total rotor power requirements, throughout the flight envelope. This will especially be so for flight cases where the flow field over the rotor blades contains strong shocks or regions of separated flow.

Viscous effects have an important role in most regions of the rotor disk. Although most predominant on the retreating blade, with large separations, viscous effects are also important in high-speed flight where they affect the shock position and thus moment predictions.

In order to obtain an adequate estimate of the torque and improved moment predictions as required in a coupling with comprehensive codes ,a medium level of the viscous-inviscid interaction approach (VII) is developed, which applies time-consistent coupling restricted to attached flow and further assumes an unsteady locally-2D viscous solution, given by the VIS05 code developed at ONERA , implemented in a stripwise fashion.

The method is described in the following sections.

3.1 Viscous numerical method

A viscous-inviscid interaction (VII) approach based on the VIS05 code developed at ONERA [16, 17, 18, 19], has been introduced in the HELIFPX code. This VIS05 part is basically issued from the common methodology of Viscous-Inviscid Solver ”VIS”, using the thin-layer approximation of Le Balleur’s ”Defect Formulation theory” for Navier-Stokes equations [16, 20, 18, 19]. This theory assumes at all points a splitting of the system of equations (RANS Navier-Stokes) in two exactly equivalent systems: The viscous ”Defect-Formulation” system and the pseudo-inviscid flow system, both being solved in the same physical domain. The advantages of the VII approach consist of a relatively low computational cost that does not grow with the Reynolds number, a much lower undesirable numerical viscosity, and a high flexibility in choosing at will the viscous approximation level, ranging from boundary layer to full RANS. A viscous interaction approach of medium level (time-consistent, attached flow) was chosen, with an unsteady locally-2D viscous solution implemented in a stripwise fashion.

The viscous numerical method [16, 18, 19, 21] is a field/integral hybrid method, based on velocity profiles discretized along the normal direction, but parametric (with an adjustable numerical rank, but lower than the discretization rank) and based on the number of unsteady integral equations necessary to the chosen parametric rank. These equations, which are obtained by integration along the normal of the local ”Defect-formulation” equations, are less restrictive than the Prandtl integral

equations. At each node, the numerical method involves a space marching technique using non-linearly implicit schemes, implicit turbulence coupling and a switch between direct and inverse mode, according to the state of the viscous layer (attached/separated). At each viscous station, "parametric" modelled turbulent velocity profiles [16, 17, 18, 19] - ranging from attached flow to massive separation - are discretized along the normal direction to the local inviscid interacting flow streamlines, on a normal grid that is self-adaptive to the boundary layer thickness and the maximal normal velocity gradient. The integral viscous quantities are obtained from the profile discretization by numerical integration. The method includes first an algebraic turbulence model [16, 18, 19, 21], based on the discretized parametric velocity profiles and on a mixing-length, and secondly an out-of-equilibrium two equation model "k-u'v' forced" [16, 18, 19, 21], forced by the parametric velocity profiles modelling.

3.2 Turbulent velocity profiles modelling

An original parametric analytical description of the mean-flow velocity profiles, suggested first in 2D, then in 3D, see [18, 20, 22], is used.

This modelling has been designed for describing the attached and the massively separated flows as well, without mathematical anomaly in viscous upstream influence and integral properties, see [22]. Let us recall that the modelling operates normal to the interacting inviscid streamlines, not normal to the wall:

$$\begin{aligned}\left(\frac{\bar{u}}{q}\right)(a,\delta,z) &= 1 - W(a).F\left(\frac{z}{\delta}\right) \\ &+ \frac{Cf}{|Cf|}(1-D).\frac{1}{\kappa}\left|\frac{Cf}{2}\right|^{1/2} Log\left(\frac{z}{\delta}\right) \\ &- (1-W(a)).D + D\frac{Cf}{2}Re_\delta\left(\frac{z}{\delta}\right)\end{aligned} \tag{1}$$

with

$$F(\eta) = \left(\left(\frac{\eta-\eta^*}{1-\eta^*}\right)^{3/2} - 1\right)^2 ,$$

where δ is the boundary layer thickness, δ^1 the displacement thickness, z the normal coordinate and $\bar{u}$ the tangential component of the viscous velocity. The independent shape parameter a is, for

example, the incompressible displacement parameter $\left(\delta^1/\delta\right)_{incompressible}$:

$$a = \int_0^\infty \left(1 - \frac{\bar{u}}{q}\right) \frac{dz}{\delta} = \left(\frac{\delta^1}{\delta}\right)_{incompressible} . \tag{2}$$

The free parameters are the 2 viscous parameters δ, a, plus the inviscid velocity q and R_θ the local Reynolds number based on ρq and δ.the tangential component of the viscous velocity. The suggested modelling of η^* is given by, see [16, 22]:

$$\eta^* = max\,[0, 2.406(a - 0.5844)],$$

with parabolic blending for:

$$\eta^*(a) \text{ on } 0.46 < a < 0.71.$$

The common point of the present velocity modelling with the Coles' idea [23] is the additive composite form (law of the wall-law of the wake), but the form has been extended here to separated flows, and the present wake models F^* and F are different.

The simple wake function of Coles would be quite unrealistic in massively separated flows (infinite velocity in reverse flows).

The modelling of $\eta^*(\delta^1/\delta)$ is deduced from the analysis of boundary layer singularities at separation, [24, 25], from the analysis of characteristic cones of the 2D/3D-equations in connection with the recovery of upstream influence in separated flows, [22, 24, 25, 19], and also from the capability of quantitatively describing the 2D mixing-layer limit in massively separated flows, [22].

The expressions of the wake coefficient $W(a)$, and of the laminar damping function D, are detailed in [18, 22]. The skin-friction Cf is deduced from the "universal" law of the wall modelling (with $\kappa = 0.41$):

$$\left|\frac{Cf}{2}\right|^{1/2} \left[Log\left(Re_\delta \left|\frac{Cf}{2}\right|^{1/2}\right) + 5.25\kappa - \frac{1}{A}\right] = \kappa. \left|\left|1 - \frac{a}{A}\right|\right|, \tag{3}$$

with

$$A = \eta^* + (1 - \eta^*) \int_0^\delta \left(\eta^{\frac{3}{2}} - 1)\right)^2 \, d\eta \ . \tag{4}$$

The compressibility does not modify the velocity profiles description. In adiabatic flows the density profiles are deduced from an isenthalpic modelling $\bar{h}_t = h_t$ (viscous enthalpy = inviscid enthalpy). The compressibility effect writes for the skin friction, denoting γ the specific heat ratio and M the Mach number:

$$Cf_{compressible} = Cf \left[1 + 0.5(\gamma - 1)M^2\right]^{-1/2} \tag{5}$$

As a final improvement used, in advanced options of the above velocity modelling, the small but non-zero $(\partial\bar{u}/\partial z)_\delta$ at $z = \delta$ of the above formulas has been fully removed, by adding to the law of the wake an opposite linear $z-$variation. Figure 1 shows the velocity profiles for the shape parameter a, varying from .1 to 1.

4 Accelerated procedures for solving the full potential equations in the outer flow

The use of HELIFPX in the design optimization of rotor blades requires relatively small turn-around times in applications.

Therefore the use of faster solution methods is exploited as the use of parallel and vector hardware is not expected to have a large effect on the performance of the applied inviscid and viscous solver because the number of independent CPU operations and the applied vector lengths are relatively small.

Basically the HELIFPX code utilizes a Newton method to solve the nonlinear discretized system from time step n to $n + 1$. An implicit approximate factorization method (AF3) is applied for solving the linear algebraic system that results at each Newton sub-iteration stage.

This solution methodology adheres to the following:

- This method has fairly good convergence properties, but it is not easy to optimize it for general configurations; factorization errors scale up with time step and the grid cell aspect ratio has a great influence due to the splitting errors.
- For hover applications, in which time-accuracy is not needed Newton iteration is not applied, variable time stepping is applied to accelerate to a steady state.
- The maximum allowable CFL number can be infinitely increased. However, eventually the convergence will degrade as the LHS departs too much from the RHS and splitting errors might dominate.

Nevertheless, applications have shown an undesired sensitivity of the AF3 method for the quality of the computational grids which lead to reduced efficiency and might hamper blade-design studies.

The efficiency is increased by development of the following methods:

Higher order temporal accuracy. The efficiency is improved for time-accurate simulations by adopting a second order approximation of the time-derivative with respect to the density which aims at:

- making a forward flight simulation with larger time steps (efficiency).
- reducing sensitivities at the start up of the Newton process (robustness).

GMRES. GMRES published in [7] is a well known efficient and robust algorithm for solving nonsymmetric matrices which is used with a limited dimension of the Krylov space to limit the linear storage and the quadratic computational cost associated with the dimension of the Krylov space. The embedding of GMRES aims at:

- Reduction of sensitiveness to grid quality (robustness).
- Increase of efficiency and robustness by reduction of factorization errors.
- Forward flight applications (efficiency).

GMRES is primary embedded as accelerator and uses either the matrix-free [26] or the AF3 preconditioned approach inside the Newton iteration loop. The latter approach freezes the linear system. The method might also be applied direct (e.g. without first applying the standard AF3 method).

Severe underrelaxation is applied when the amplitude of the first Krylov vector or the correction vector is strongly different with respect to a reference vector obtained from the previous GMRES application and/or the AF3 method. The latter might happen during start up transitions and during changes of shock positions.

Multi-grid. The well known Full Approximation Storage multi-grid (FAS-MG) algorithm [8] is embedded for preconditioning the flow field rapidly and might be worthwhile for cases involving very low frequencies (long wave) and inefficient grids. The approach is the fastest and will increase robustness on inefficient grids.

The method is primary directed to steady (hover) state applications. The method is implemented such that time-accurate simulations might be carried out with the algorithm in the near future. However, full implementation and verification of the latter possibility is not carried out within the ROSAA project. [1]

The embedded multi-grid scheme, consist of three important operators:

1. The prolongation operator (interpolation) takes care of the transformation of the solution on a certain coarser grid level to a finer grid level. Tri-linear interpolation in computational space is applied. During the verification it turned out that this can lead to unrealistic physical stages near the blade tip when interpolating a solution from a coarser grid to the next finer one. Therefore the tri-linear interpolation is modified with a volume weighting to take account of cell metrics.
2. The restriction operator is responsible for the transformation of the solution to a coarser grid level. Fully weighted restriction operators are applied to the mass and far field equations which mimics the transpose of the prolongation operator. Injection is applied to the wake and slit equations.
3. The smoothing (relaxation) operator consists of the AF3 method and a RBK method[2]. The RBK method applies implicit solving along the k direction, with a red-black (i, j)

[1] Preliminary experience with time-accurate full potential multi-grid applications has revealed that the smoothing performance of the AF3 method is not adequate near the trailing edge zone and in supersonic zones. Local application of GMRES will probably resolve this problem.

[2] Direct solving is applied when the number of unknowns is smaller than a treshold.

ordering strategy. During the verification it turned out that the smoothing properties of the AF3 method using a global time step were not sufficient. Therefore local-time stepping (LTS) has been introduced to increase the smoothing performance. Also to prevent the occurrence of odd-even type oscillations that sometimes showed up the corrections on coarse grids are smoothed with an implicit smoother before prolongation takes place. Then smoothing properties are increased by modification of the AF3 method to account for large aspect ratio effects. Finally in supersonic parts it turned out being necessary to add explicit time-like damping terms [27] for stability.

The following remarks apply further to the embedding:

- The entropy and viscous corrections are not applied on the coarse grid levels.
- A V-cycle strategy is used.
- The coarse grids satisfy: $N_{L-1} = \frac{N_L}{2} + 1$, where N denotes the number of mesh points in each direction. When the grid cannot be bisected, one plane is deleted for allowing at least one coarsening.

5 Grid Generation

Grid generation is performed with the VIS12.GRID code of ONERA [28, 1] which is an automatic special-purpose algebraic grid generator for generating single-block standard grids of CH topology with high resolution and quality, both for periodic and non-periodic blades.

Special care is taken in the development of the following features:

User interface and visualization. To increase the userfriendliness and to have easy access to visualization the VIS12.GRID code has been embedded in the GEROS grid generator. The grid generator GEROS, developed within the Brite/EuRam EROS project, deals with the complete dynamic geometrical problem raised by CFD application for rotorcraft blades: surface grid generation, volume grid generation, volume grid adaptation/ deformation/ rotation/ positioning, dynamic connectivity and animation/prototyping of the dynamic geometries.

Grid adaptation for complex tip shapes. The VIS12.GRID module has been extented for blades with a tip shape with a chord length approaching zero.

Grid adaptation for acoustic postprocessing. The VIS12.GRID module supports the tailoring of the grid near the tip for obtaining an adequate prediction of acoustics in the far field as the latter is sensitive to specific criteria of grid-quality based on the orientation of the grid at the outboard tip in the direction of acoustic propagation.

The resulting grid generation system is called GEROSV. The following sections present details concerning VIS12.GRID.

5.1 VIS12.GRID generation

The grid generator VIS12.GRID was first developed specifically in advanced Viscous-Inviscid Methods, [16, 19], for wings, and then applied to helicopter rotors (code VIS12) [19]. It is built to have a cheap CPU-cost ”fire-and-forget” execution, fully automatic and very rapid in terms of man-power, based on the input of a selected number of command parameters, that are dedicated, and single targeted ones. A finer adaptation of this code was developed in the HELISHAPE project, and new extensions have improved again VIS12.GRID in the ROSAA project.

5.1.1 Complex blade planforms

Improvements have been introduced by studying a better choice of the outer-blade CH-cut geometry in case of complex blades with narrow blade-tips. The outer-cut has been made dependent, not only on the distance to the rotation-axis and on the extreme chord length at the blade-tip, but also on the averaged swept-angle and taper-ratio of the blade-tip, as provided by the geometry-data in

the final sections near tip.

5.1.2 Aeroacoustic improvement

The major point is in the improvement of the outer-blade CH cut geometry, for which the leading-edge planform has to follow the lines of relative Mach number, as induced by blade rotation.

Denoting r, φ the polar coordinates in the planform plane, s_{le} the curvilinear abscissa along the leading edge of the cut, R the rotor radius:

$$r_{le}.d\varphi_{le} = ds_{le}.\cos\beta$$
$$dr_{le} = ds_{le}.\sin\beta$$
$$\sin\beta = \frac{1}{M_{le}} = \frac{1}{\max(1.,\mathrm{M_R}\frac{r}{R})}$$

An azimuthal shift $\varphi_{le}(r)$ of the grid at large r has been introduced for the far-field. An example of an adapted mesh for the UH-1H rotor in hover configuration at a tip Mach number of 0.95 is shown in figure 2.

6 Applications

The HELIFPX code has been verified on many test cases, covering the entire operating regime of a helicopter, *i.e.*, both lifting and non-lifting hover and forward flight conditions. Moreover, airfoil and fixed wing test cases were added for both steady and unsteady conditions.

This section presents a selected set of results, obtained at the end of the contract period (June 2000), demonstrating the proper functioning of the code implementations for:

Airfoil: The NAC0012 airfoil in a transonic steady and unsteady condition;
Fixed Wing: The LANN wing in a transonic steady and unsteady condition;
Rotors

1. The Caradonna Tung rotor in a subsonic steady hover condition;
2. The BO-105 rotor in a subsonic forward flight condition;
3. The EC/ONERA 7A rotor in a low speed forward & level flight condition.

The results are presented in the form of pressure distributions, convergence characteristics and inflow distributions.

6.1 2D NACA0012 applications

In this section the NACA0012 airfoil is considered. We consider the steady cases: Mach = 0.63, $\alpha = 2$ degrees; Mach = 0.8, α = 1.25 degrees and the well documented AGARD CT5 case: Mach = 0.755, α = 0.016 degrees, $\Delta\ \alpha = 2.51$ degrees where the airfoil motion is pitching about the quarter chord point at a reduced frequency of 0.0814.

6.1.1 Subsonic inviscid flow around NACA 0012 airfoil

Calculations are performed for the well known subcritical case Mach = 0.63 with α = 2 degrees. The standard AF3 method is applied and the FAS-MG method.

The grid has been generated with GEROSV with dimensions 192 * 64 to suit the needs of the FAS-MG method.

Convergence characteristics $||R.c||_1$ and $C\_L = ||\phi||_{te}$ are depicted in figure 3 versus CPU time [1]. The weighted 1-norm $||R.c||_1$ is a more objective norm in measuring convergence as it might be considered as an analogy to the amount of remaining energy in the system $(E = R.c)$. It is

[1] CPU time is measured on a SG O2 machine with 225MHZ IP32 processor.

defined as:

$$||R.c||_1 = \frac{\sum_{i=0\ j=0\ k=0}^{i=ni\ j=nj\ k=nk} |R|.|c|}{(ni+1)(nj+1)(nk+1)},$$

where R denotes the residual and c the associated correction. Results of the FAS-MG method using 1 and 2 cycles (3 fine mesh updates) are shown. Convergence of the FAS-MG solver is very fast. Some oscillations are noticeable after the first V-cycle which disappear after the second.

The pressure coefficients (C_p) are depicted in figure 3 as obtained at the final iterations of the solvers. The FAS-MG results are fairly close to the AF3 ones.

6.1.2 Transonic flow around NACA 0012 airfoil

This section presents viscous results of the HELIFPX code for the NACA0012 airfoil in a strong transonic condition: Mach = 0.80, α = 1.25 degrees and Reynolds = 3.8 Million. The grid has been generated with GEROSV with dimensions 160 * 23. The effect of viscosity on the pressure coefficient is demonstrated in figure 4. The viscous predictions which correspond to attached boundary layer flow are relative insensitive to the update frequency of the non-linear boundary-layer (ITS) and the applied turbulence models (MDL, 0 = algebraic, 2 = two-equation "$k-\omega$"). A large difference is observed between the viscous and the inviscid prediction with the entropy correction model activated.

6.1.3 Unsteady Transonic flow around oscillating NACA 0012 airfoil

Unsteady calculations have been performed to verify the GMRES solver, the second order time accuracy and the viscous model. Two cycles of oscillations have been applied and various settings of the time step and solvers have been investigated. The grid oscillates rigidly with the airfoil. All results have been started from the same steady flow field which has been obtained at the end of the AF3 method iterations. Inviscid and viscous pressure coefficient (C_p) predictions are depicted in figure 5. The figure clearly demonstrates that 72 time steps in a cycle is insufficient for capturing the pressure in the shock trajectory with 2 subiterations. At this time step the results already show a grid related undulating effect in the superzonic zone. The effect of second order time accuracy turned out to be significant here, especially in the subsonic region. Note also the strong peaks at the trailing edge. At the high setting of 576 time steps in a cycle results are converged. It turned out that 288 time steps in a period is a minimum requirement to capture the pressure on this grid with 2 subiterations. The GMRES application at 72 time steps in a period presents results much closer to the reference solution as the AF3 result. It does not show the oscillating behavior and it reduces the peak values at the trailing edge. Due to the fact that the viscous predictions have been obtained with the 'time-consistent coupling' (TCV), they are relative insensitive to the number of

time steps applied in the inviscid solver. Viscous effects are relatively more pronounced in the supersonic zone. The mean and the imaginary part are hardly effected.

6.2 3D LANN wing

In this section the LANN wing is considered. We consider the case: Mach = 0.822, α = 0.6 degrees, $\Delta\,\alpha$ = 0.25 degrees where the wing motion is pitching about the 62.1% root chord position at a reduced frequency of 0.102. The geometry is typical for a transport aircraft wing oscillating in the transonic regime near flutter conditions. The flow field is characterised by rapid shock motion during the wing oscillation cycle and is highly unsteady. The LANN wing test case [29] has been widely used in the past to validate CFD unsteady transonic codes. The grid[2] has dimensions 120*31*23 which are not particularly well suited for multi-grid applications. It can only bisect once in the j and k direction and twice in the i direction.

A comparison of the convergence of the solvers for Mach = 0.822, α = 0.6 degrees is shown in figure 6 and a comparison of steady pressure distributions is presented in figure 7. Convergence characteristics $C\_L = ||\phi||_{te}$ and the development of the supersonic points are depicted in figure 6 versus CPU time. The figures compare convergence characteristics for several settings of the solver. The FAS-MG seems to converge the fastest, but needs more iterations as compared to the 2D subsonic case. The latter is most probably due to the grid dimensions which are not suited to the MGFAS solver.

Pressure coefficients (C_p) are depicted in figure 7 at selected span stations as obtained at the final iterations of the solvers. The GMRES results are very close to the AF3 ones. The FAS-MG results are very close to the other inviscid results, except in the shock areas, and are within engineering accuracy. A large difference is observed between the viscous (Reynolds = 6.1 Million) and the inviscid prediction in the shock trajectory. The shock is weakened both in terms of position and strength. The application of one boundary-layer update per time step turned out to be sufficient.

Unsteady calculations have been performed to verify the GMRES solver, the second order time accuracy and the viscous-inviscid coupling. Two cycles of oscillations using 180 time steps in a cycle have been applied using 2 subiterations and various settings of the solvers have been investigated. The grid oscillates rigidly with the wing. All results have been started from the same steady flow field which has been obtained at the end of the steady application of the AF3 method.

[2] Introduced in [30] and applied in [1, 4] for validation purposes.

Pressure coefficients (C_p) are depicted in figure 8 for selected span stations. The figures show inviscid results of the AF3 and GMRES solvers. They clearly demonstrate that 180 time steps in a cycle is insufficient for capturing the pressure properly in the supersonic part of the flow with the AF3 method. Also the effect of second order time accuracy is significant here. The GMRES solvers present results without oscillations.

The effect of viscosity is demonstrated in figure 8 too for the same case with Reynolds = 6.1 Million using the same grid with and without time-consistent updating (invocation of time-consistency is a factor 20-30 more expensive).

The shock peaks are strongly reduced and shifted upstream. The pressure distribution at the low-erside is only influenced near the trailing edge. The oscillations in the supersonic zone which are the results of an inadequate time step are not reduced when the viscous model is used without invocation of time-consistency. The mean pressure coefficient is hardly sensitive to the viscous updating procedure and the same holds for the first harmonic pressure distribution aft of the shock.

6.3 3D rotary wings

Results obtained for rotor blades in hover are presented first. Then results for forward flight will be presented.

6.3.1 Hover

In this section the Caradonna-Tung rotor is considered. We consider the hover case: $M_R = 0.61$ and a collective pitch angle $\theta = 5$ degrees. First results obtained with the BEM modelling are presented in Fig. 9, which gives a comparison of calculated prescribed wake, free wake and experimental [31] pressure distributions at selected span-stations. The agreement between the predicted and experimental data is satisfactory. The solution obtained by a free-wake analysis is closer to the experimental data than the one obtained by the prescribed helicoidal wake[3].

Figure 10 presents a comparison of calculated inflow at the induction points located at $x/c = 0.25$ on the blade section. Seven types of results are compared: (L&R1) free-wake, (L2) Landgrebe wake, (L3) Tung wake , (R2) MOMENTUM +BL.EL, (R3) RAMSYS [32] and (R4) GWHL[4]. The first three wake models are fairly close. There is a larger difference between the free wake and the other results, especially at the tip. The free-wake model seems to be the better one. The presence of the bump at the tip should be considered as an improvement. For it is to be expected due to the

[3] Three wake spirals were applied which is more than sufficient.

[4] provided by GKN-WESTLAND.

fact that the tip vortex moves towards the rotor axis. Vice versa, using a spiral wake model, which has no tip–vortex "constriction", one obtains results without the bump.

Next, calculations are presented that have been obtained with the full potential model method for the same case. No induced wake model or boundary layer model is applied. The grid dimensions (160 x 32 x 40) are well chosen for multi-grid applications. Convergence characteristics $||R.c||_1$ and $C\_L = ||\phi||_{te}$ are depicted in figure 11 versus CPU time. The figure compares convergence characteristics for the AF3 and the FAS-MG solver. The latter method clearly converges faster. Pressure coefficients (C_p) are also depicted in figure 11 at selected span stations as obtained at the final iterations of the solvers.

Next, figure 12 shows a comparison of calculated viscous and inviscid pressure coefficient distributions at $M_{\omega R} = 0.61, \theta = 12$ degrees. and Reynolds = 7 Million, based on the blade radius on the same grid. No inflow model has been applied. The viscous effects are very small, except for the zones near the trailing-edge, the leading-edge and the shock waves.

6.3.2 Rotors in forward flight conditions

The BEM modelling has been applied to simulate the pressure coefficient distribution on a four-bladed BO-105 main-rotor with pitching motion (HELINOISE test Datapoint 34/508, Ref. [33]).

Figure 13 (top and middle) presents results obtained for two spanwise sections at $r/R = 0.75$ and $r/R = 0.87$, both at $\Psi = 0$ degrees and at $\Psi = 120$ degrees with the prescribed wake and the free wake methods. These results are compared with experimental data. The number of wake spirals has been varied between 1.5 (BEM_NEW = 18) and 3 (BEM_NEW = 36). It can be concluded that the behaviour of the solution is the same and that the effects of the prescribed wake can be fully captured by using two wake spirals. The agreement between the numerical results and the experimental data is fairly good. The free wake compares slightly better.

Finally, figures 14 through 21 report a numerical sensitivity study conducted for the EC/ONERA 7A rotor for a low speed forward & level flight with advance ratio $\mu = 0.167$, $C_T/\sigma = 0.0815$ and rotational velocity $M_{\omega R} = 0.616$ [5]. Aeroelastic deformations are not considered and trim conditions were not applied. The blade motion, which is mainly blade pitch, is in accordance with the experiment carried out in the HELISHAPE project [34].

First, figure 14 shows comparisons of calculated pressure coefficient distributions at the 60 degrees

[5] C_T = thrust coefficient and σ is the rotor solidity.

azimuthal station for selected radial stations. The figure demonstrates the effect of time step ($\frac{2\pi}{GNRTS}$) using second order temporal accuracy and 2 subiterations. Only the AF3 method is applied on a grid with dimensions 90 x 35 x 49. The effect of time step ($\frac{2\pi}{GNRTS}$), temporal order of accuracy, number of subiterations and entropy correction have been studied (not shown here) and revealed that results are converged applying 2 subiterations. The effect of applying second order accurate temporal discretization turned out to be marginal, although favourable, and only significant at the outboard sections and the larger time steps. The entropy correction had no effect at all since no strong shocks occur. According to the results, a time step of 0.5 degrees should be chosen as the correct value for subsequent simulations on this grid. A larger value would give output results dependent on the spatial approximation chosen by the user, while a smaller one would not affect the final results but would require higher CPU-times.

Then, figure 15 shows comparisons of calculated pressure coefficient distributions and the effect of the spanwise grid distribution at tip (RSTIP) and hub (RSHUB) at the $r/R = 0.98$ blade station and selected azimuthal stations. The grid distributions have no visible effect at the more inboard stations and the effects are relatively small, but present, at the $r/R = 0.98$ blade station.

Next, figure 16 shows comparisons of calculated pressure coefficient distributions involving the effect of the number of grid planes at the $\Psi = 90$ degrees azimuthal station for selected radial stations. The grid distributions have a relatively small effect except for the coarsest grid.

Figure 17 shows the convergence characteristic $||c||_\infty$ of the AF3 method with respect to the number of Newton subiterations versus the iteration count ($\Psi = \frac{Iteration}{2}$ degrees and $\Psi = \frac{Iteration}{4}$ degrees for the left and right figure, respectively).

The application of a higher number of subiterations has a relative small effect on the convergence level which might be caused by the application of single precision. The convergence level remains bounded during the unsteady simulations.

Finally, the GMRES and the FAS-MG solution procedures are demonstrated for the same case. Figure 18 and 19 show comparisons of calculated pressure coefficient distributions at selected radial and azimuthal stations demonstrating the effect of time step ($\frac{2\pi}{GNRTS}$) and the GMRES accelerator using second order temporal accuracy and 2 subiterations. 4 Krylov vectors are applied. The grid had dimensions 90 x 40 x 56. According to the results, a time step of 1 degrees is adequate when the GMRES method is used (MYGMRS, 0= AF3 preconditioned). The largest sensitivities occur at the outboard station and at the $\Psi = 60$ degrees azimuthal angle.

Figure 20 shows the convergence characteristic $||c||_\infty$ of the various methods during the steady start up procedure with respect to the iteration count (number of pseudo-time steps). A variable time step was applied in accordance with a CFL number variation between 10 and 100.

The application of FAS-MG (MGFS, 0 = (on), 1 = (on & full multi-grid)) and GMRES has a strong and favorable effect on the convergence level. The stagnation in the convergence of the GMRES method is simply due to the fact that the latter method is not invoked when the correction is smaller than a tolerance (1.E-6).

Figure 21 shows the convergence characteristic $||c||_\infty$ of the GMRES and the AF3 methods with respect to the number of subiterations versus Ψ. The convergence level remains bounded during the unsteady simulations and GMRES converges better at the second Newton iteration. It should be noted that the GMRES results refer to a time step of 1 degrees and the AF3 refer to a time step of 0.5 degrees. The latter explains the relatively small increase of the correction at the first Newton iteration.

The figures demonstrate that the results for practical purposes might be considered as relatively insensitive to most of the parameters studied.

7 Conclusions

Recent developments have been presented with respect to a potential flow approach, a viscous-inviscid interaction method, a free-wake boundary element model and a grid generator which are deployed to model the flow about complex multi-bladed rotors.

These aerodynamic components form an essential part of a complete rotorcraft simulation method, the Brite/EuRam ROSAA system that aims at enabling routine CFD applications of high quality coupled to comprehensive rotor codes for the efficient prediction of aerodynamic quantities of interest (blade loads, blade torque etc) over a wide range of flight conditions, from hover to high-speed forward flight.

This work comprised the following activities:

1. The viscous part of an existing inviscid/viscous interaction method based on an unsteady, locally 2D, field integral approach has been coupled in a stripwise fashion in the full potential flow solver.
2. A methodology for the evaluation of a fixed and a free-wake inflow model based on a boundary element approach to solve the incompressible and the linear compressible potential flow has been developed, and coupled to the full potential solver.
3. The full potential solver is improved by: enhancement of temporal accuracy to second order, development of a linear and a nonlinear Krylov accelerator of generalised minimal residuals (GMRES) for forward flight and development of a full approximation storage multi-grid accelerator (FAS-MG) for hover simulations.
4. The automatic special-purpose algebraic grid generator for single block grids (VIS12.GRID) method is equipped with new possibilities tailored to acoustic requirements, and integrated with the system.

From analysis of results of applications for 2D airfoils, 3D wings and rotary wings the following conclusions can be drawn:

- The Laplace and Helmholtz equation based free and fixed wake inflow models have successfully been verified for rotors in hover and in forward flight. Predicted pressure distributions and inflow compare fairly well with experimental data and other theories.
- The embedding of the viscous correction model has shown the importance of modelling viscous effects in transonic flow and can be used for 2D and 3D flows with shocks up to incipient separation. The time-consistent modelling is important for the adequate modelling of the unsteady flow in supersonic zones.

- The increase of efficiency and robustness has been demonstrated for a 2D airfoil, a fixed wing and rotors. FAS-MG is very efficient for subsonic flows and the GMRES acceleration enhances robustness in all cases studied here. The increase of the temporal accuracy has a relatively small effect on the results at the relatively small time step which is required to obtain convergence with the approximate factorization based full potential equation solver (AF3) in supersonic zones.
- The grid generation effort is reduced due to the userfriendly interface, the visualizaton and the high quality of the grids produced by the automatic grid generation module.

8 Acknowledgments

This work is partially supported by the European Union under the Brite-EuRam Contract No. BRPR-CT98-0622 (ROSAA project). The authors would like to thank A. Pagano, J.V. Miller, A. Kokkalis and L. Morino for their continuous support and B. Oskam & O.J. Boelens for contributions to this paper.

9 References

1. M. Costes, J.C. Le Balleur, L. Gasparini, L. Vigevano, M.H.L. Hounjet, A. Kokkalis, J.V. Miller, M. Spruce, A. Pagano, P. Renzoni, A. Rocchetto, and F. Toulmay. Development of a Common European Unsteady Full Potential CFD Code for Helicopter Rotors in Hover and Forward Flight. In *Proceedings of the 53rd Annual Forum of the American Helicopter Society*, Virginia Beach, VA, April 1997.
2. J.V. Miller, P. Difrancescoantonio, A. Pisoni, A. Pagano, M. Pidd, H. Haverdings, D. Blaise, G. Bernardini, and M. Gracey. ROSAA: The European Solution to Connect Aeroelasticity, Aerodynamics and Acoustic Codes in a Unique User-Friendly Rotorcraft Simulation System. In *Proceedings of 26th European Rotorcraft Forum*, TheHague, Sept 2000.
3. J.C. Le Balleur. New possibilities of viscous-inviscid numerical techniques for solving viscous flow equations, with massive separation. Proceed. Fourth Symp. Numerical-Physical Aspects of Aero. Flows, Long-Beach, USA, Jan. 16-19, 1989, Selected papers, chap. 4, p. 71-96, Cebeci ed. Technical Report Springer-verlag (or ONERA TP 1989-24)., 1990.
4. P. Renzoni and et al. EROS: A European Euler Code for Helicopter Rotor Flow Simulations. In *Proceedings ICAS 1998 CONGRESS, Melbourne*, number ICAS-98-2.6.2, Sept 1998.
5. Hounjet M.H.L. and Eussen B.J.G. Outline and application of the NLR aeroelastic simulation method. ICAS Paper 94-5.8.2 also NLR TR 94422, ICAS, September 1994.
6. J.C. Le Balleur and P. Girodroux-Lavigne. Calculation of Dynamic Stall by Viscous-Inviscid Interaction over Airfoils and Helicopter-Blade Sections. Technical Report Proceedings of the American Helicopter Society 51st Annual Forum, 1995.
7. Y. Saad and M.H. Schultz. A generalized minimum residual algorithm for solving nonsymmetric linear systems. Technical Report SIAM J.Sci.Stat.Comp. Vol 7, pp 856-869, 1986.
8. A. Brandt. Guide to multigrid development In: Proceedings Multigrid methods, Köln-Porz,1981, Ed: W. Hackbush and U. Trottenberg. Technical Report Springer Verlag pp 220-312., 1982.
9. M.H.L. Hounjet, C.B. Allen, L. Vigevano, N. Trivellato, A. Pagano, A. D'Alascio, and N. Jobard. Outline and Application of GEROS: A European Grid Generator for Rotorcraft Simulation Methods. In *Computational Fluid Dynamics'98*, volume 1, ECCOMAS'98 Conference, Athens (Greece), September 1988. John Wiley & Sons also NLR TR 98265.
10. A. Pagano, M.H.L. Hounjet, J.V. Miller, M. Gracey, and A Pisoni. ROSAA: A European Simulation System for the Multidisciplinary Numerical Prediction of Rotor Phenomena. In *Proceedings of ECCOMAS 2000*, Barcelona, Sept 2000.
11. L. Morino. A General Theory of Unsteady Compressible Potential Aerodynamics. Technical Report NASA CR 2464, 1974.

12. L. Morino and B.K. Bharadvaj. A Unified Approach for Potential and Viscous Free-Wake Analysis of Helicopter Rotors. Technical Report Vertica, Vol. 12, No. 1/2, pp. 147-154, 1988.
13. A.J. Landgrebe. An Analytical Method for Predicting Rotor Wake Geometry. Technical Report Journal of the American Helicopter Society, Vol. 14, No. 4, October 1969.
14. A.J. Landgrebe. An Analytical and Experimental Investigation of Helicopter Rotor Hover Performance and Wake Geometry Characterictics. Technical Report USAAMRDL Technical Report 71–24, Eustis Directorate, U.S. Army A, 1971.
15. T.A. Egolf and A.J. Landgrebe. Helicopter Rotor Wake Geometry and its Influence in Forward Flight. Technical Report Vols. 1 and 2, NASA CR 3727, 1983.
16. J.C. Le Balleur. Strong matching method for computing transonic viscous flows including wakes and separations. Lifting airfoils. Technical Report La Recherche Aérospatiale 1981-3, p.21-45, English and French, 1981.
17. J.C. Le Balleur. Viscous-inviscid flow matching : Numerical method and applications to two-dimensional transonic and supersonic flows. Technical Report La Recherche Arospatiale 1978-2, p.67-76, French, or English tra, 1978.
18. J.C. Le Balleur. New possibilities of viscous-inviscid numerical techniques for solving viscous flow equations, with massive separation. Technical Report Proceed. Fourth Symp. Numerical-Physical Aspects of Aero. Flows,, 1989.
19. J.C. Le Balleur. Viscous-inviscid calculation of high-lift separated compressible flows over airfoils and wings. Technical Report Proceedings AGARD-CP-515, Paper 26, Symposium AGARD/FDP High-lift, 1992.
20. J.C. Le Balleur. Numerical viscous-inviscid interaction in steady and unsteady flows. Technical Report Proceed. 2nd Symp. “Numerical and Physical Aspects of Aerodynami, 1983.
21. J.C. Le Balleur and P. Girodroux-Lavigne. A semi-implicit and unsteady numerical method of viscous-inviscid interaction for transonic separated flows. Technical Report La Recherche Arospatiale 1984-1, p.15-37, English and French edi, 1984.
22. J.C. Le Balleur. Viscous-inviscid interaction solvers and computation of highly separated flows. Technical Report Symposium ICASE, NASA Langley, USA, Proceed., July 1985.
23. D.E Coles. The law of the wake in turbulent boundary layers. Technical Report JFM, Vol. 1, part 2, 1956.
24. J.C. Le Balleur. Viscous-inviscid flow matching : Analysis of the problem including separation and shock waves. Technical Report La Recherche Arospatiale 1977-6, p.349-358, French, or English t, 1977.
25. J.C. Le Balleur, R. Peyret, and H. Viviand. Numerical studies in high reynolds number aerodynamics. Technical Report Computers and Fluids, Vol. 8, n^o 1, p. 1-30, March 1980.

26. C.B. Wigton, N.J. Yu, and D.P. Young. GMRES acceleration of Computational Fluid Dynamics Codes. Technical Report AIAA-paper 85-1494, DENVER., 1985.
27. D. A. Caughey. Multi-grid calculation of three-dimensional transonic potential flows. Technical Report AIAA paper 83-0374, Jan 1983.
28. J.C. Le Balleur. Viscous-inviscid calculation of high-lift separated compressible flows over airfoils and wings. Technical Report Proceedings AGARD-CP-515, Paper 26, Symposium AGARD/FDP “High-li, 1992.
29. R.J. Zwaan. LANN-Wing in Pitching Oscillations. In *Compendium of Unsteady Aerodynamic Mesurements*, number AGARD-R-702, London, UK, August 1982.
30. B.B. Prananta and M.H.L. Hounjet. Aeroelastic Simulation with Advanced CFD Methods in 2D and 3D Transonic Flow. Technical Report In Proceedings Conference on Unsteady Aerodynamics, RAeS, London, July 17-18 1996.
31. F.X. Caradonna and Tung C. Experimental and analytical studies of a model helicopter rotor in hover. Technical Memorandum 81232, NASA, September 1981.
32. A. Visingardi, A. D’Alascio, A. Pagano, and P. Renzoni. Validation of CIRA’s rotorcraft aerodynamic modelling system with DNW experimental data. In *Proceedings of 22th European Rotorcraft Forum*, Brighton, Sept 1996.
33. W. Splettstoesser, B. Junker, K.-J. Schultz, W. Wagner, W. Weitemeyer, A. Protopsaltis, and D. Fertis. The HELINOISE aeroacoustic rotor test in the DNW–test documentation and representative results. *DLR-Mitt* 93–09, DLR, September 1993.
34. K.-J. Schultz, W. Splettstoesser, B. Junker, W. Wagner, E. Schoell, G. Arnaud, E. Mercker, K. Pengel, and D. Fertis. A Parametric Wind Tunnel Test on Rotorcraft Aerodynamics and Aeroacoustics (HELISHAPE) - Test Documentation and Representative Results. Internal Report IB 129-96/25 (HELISHAPE Deliverable HELI/R/5/DLR/06), DLR, June 1996.

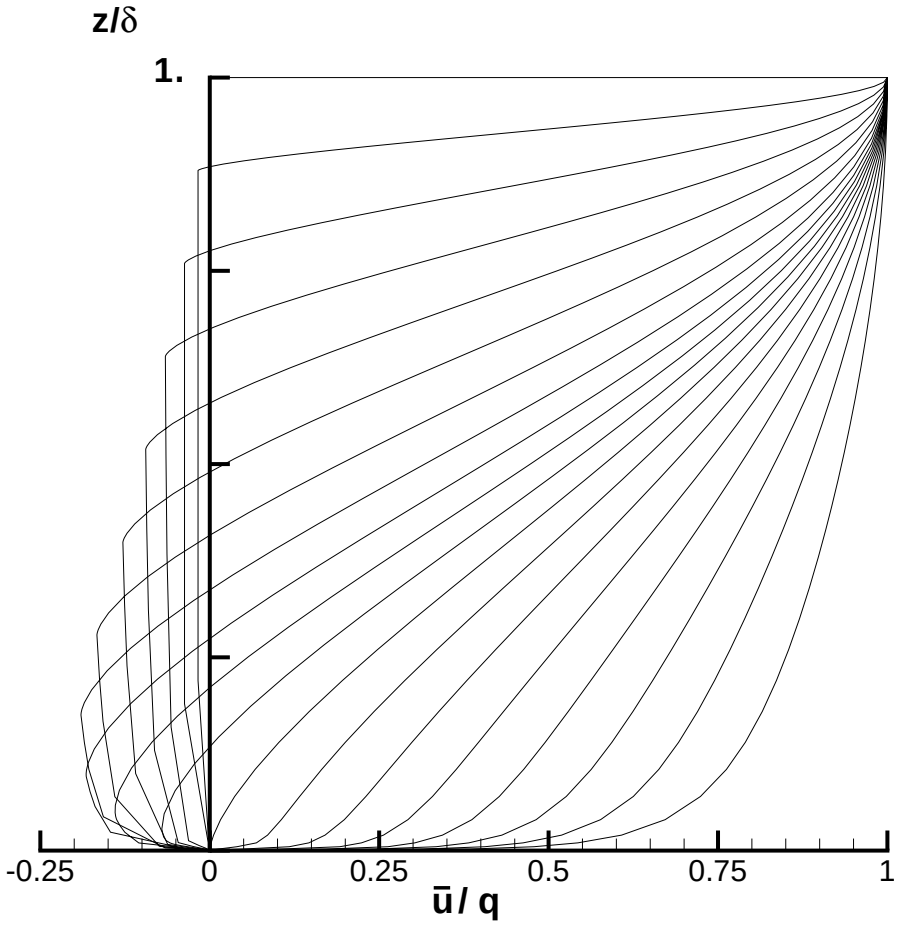

Fig. 1: Family of turbulent velocity profiles with single shape parameter a

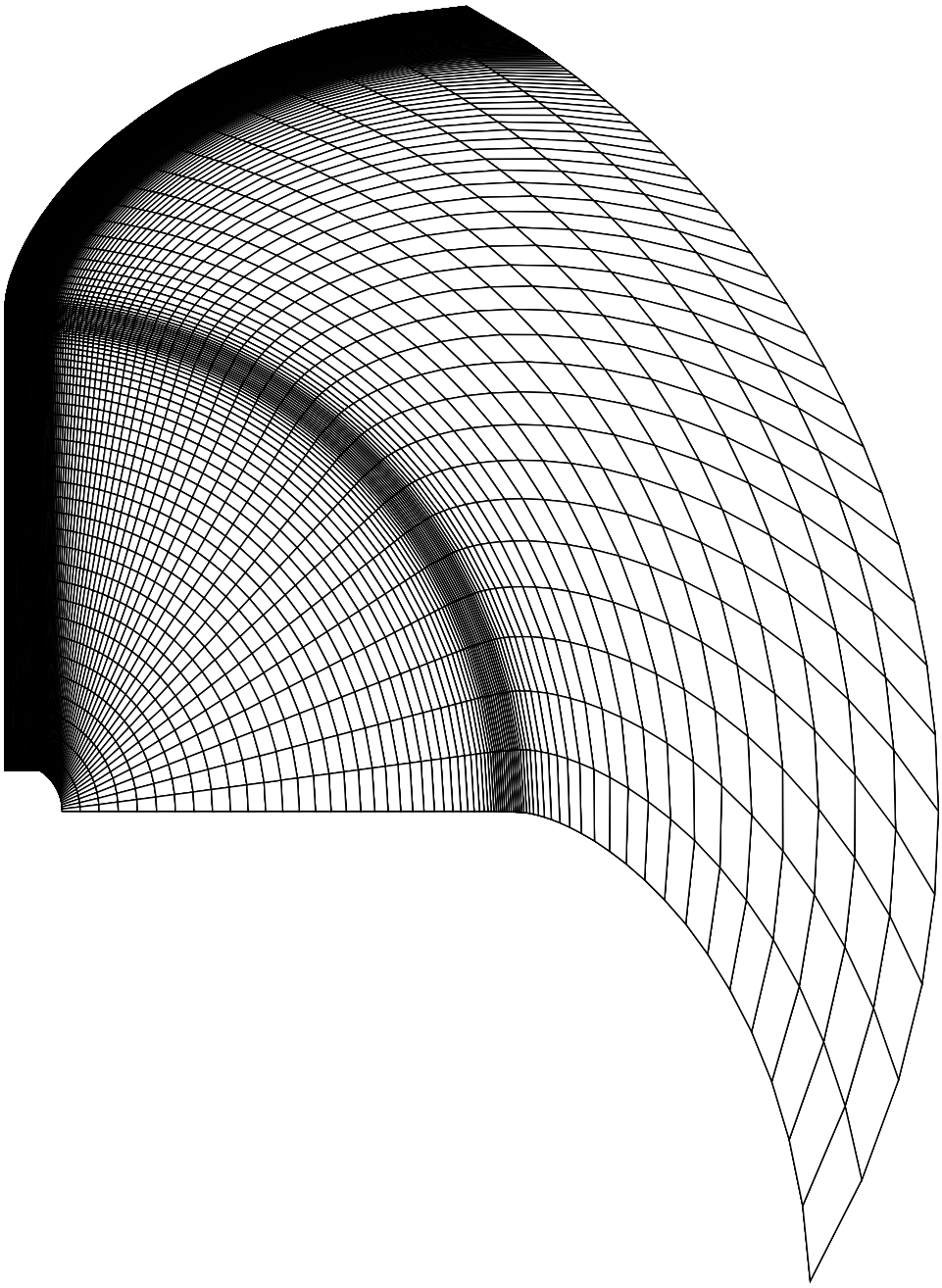

Fig. 2: Adapted mesh for UH-1H Rotor

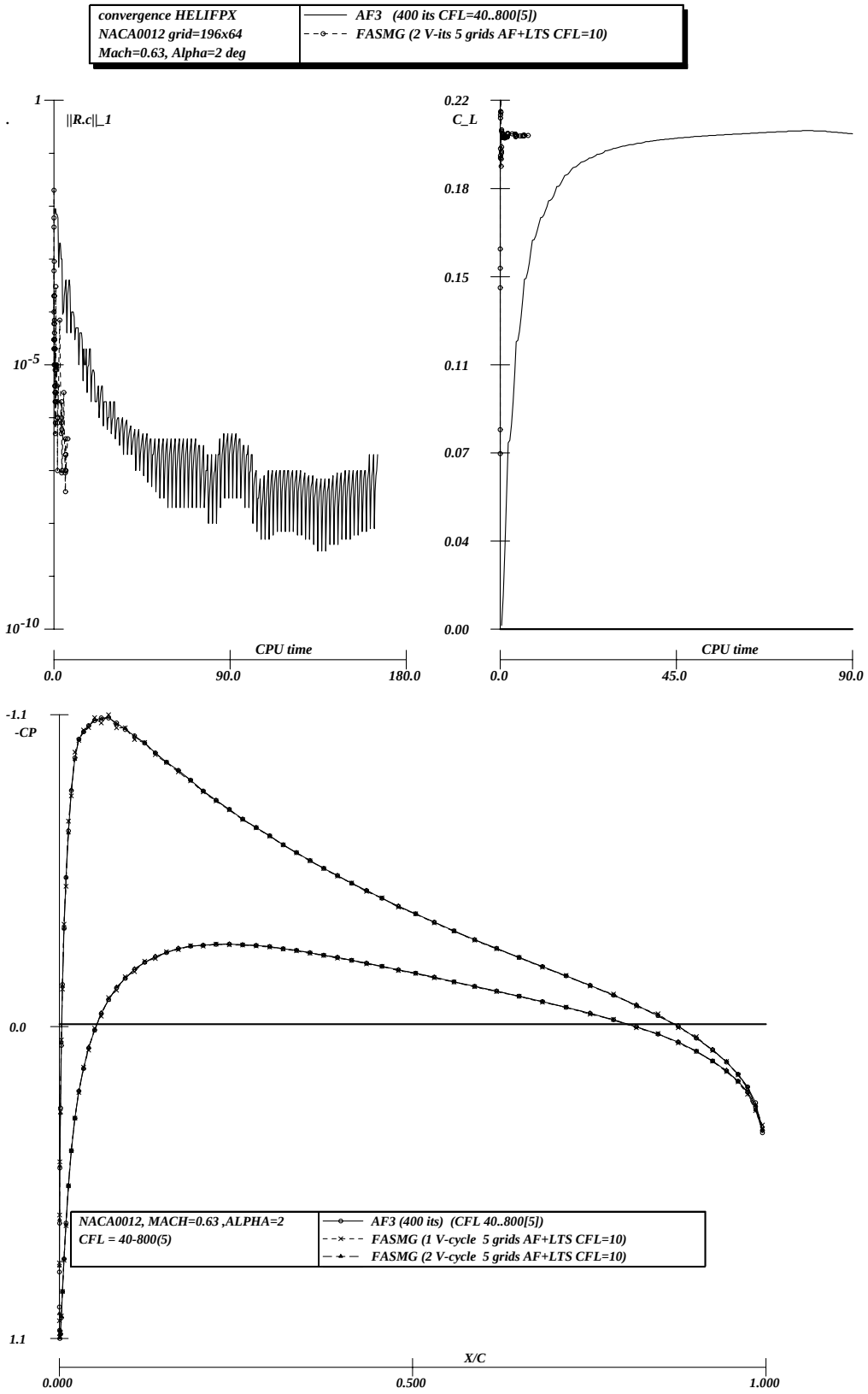

Fig. 3: Convergence characteristics and comparison of pressure coefficients for NAC0012 airfoil at a subsonic lifting condition (Mach = 0.63, α = 2 degrees); AF+LTS means application of AF3 with local time stepping

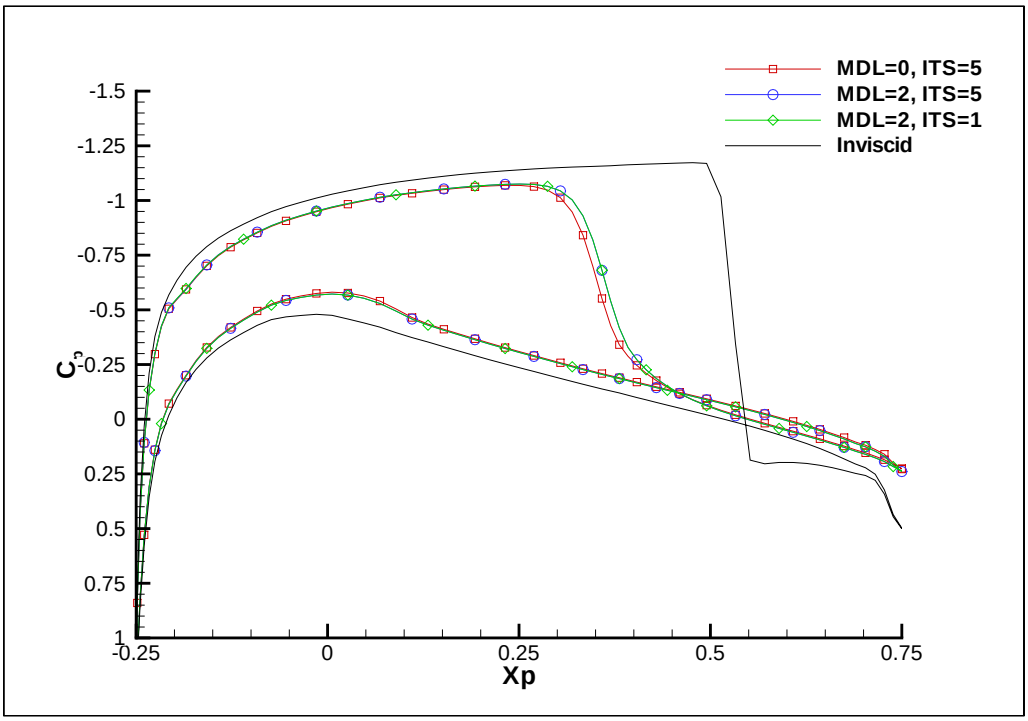

Fig. 4: Comparison of pressure coefficients for NAC0012 airfoil at Mach = 0.80, α = 1.25 degrees and Reynolds = 3.8 Million; MDL means turbulence model, ITS means boundary layer update frequency

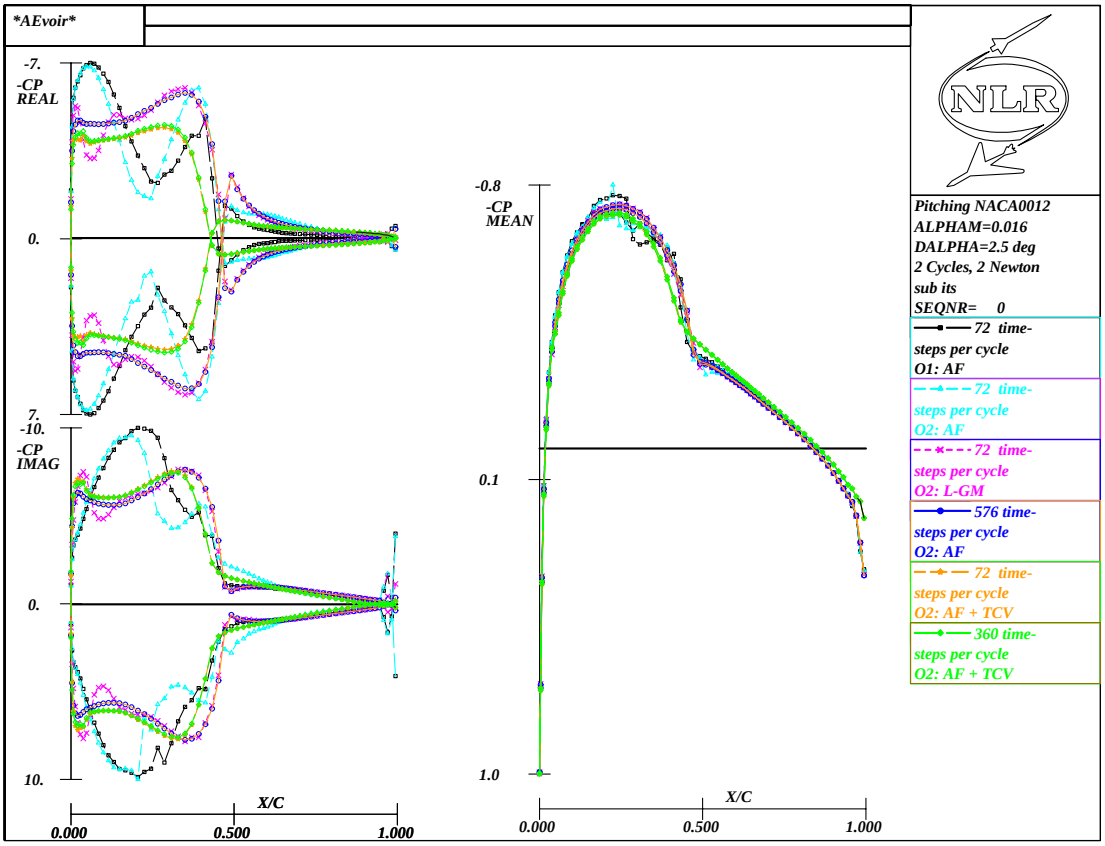

Fig. 5: Comparison of first harmonic (left) and mean (right) pressure coefficients for a pitching NAC0012 airfoil at Mach = 0.755, α_{min} = -2.34 degrees, α_{max} = 2.66 degrees, k = 0.081 and Reynolds = 5.9 Million; AF means AF3 application, L-GM means application of AF3 preconditioned GMRES, O1 and O2 mean first and second order temporal accuracy, respectively, TCV means time-consistent coupling with boundary layer

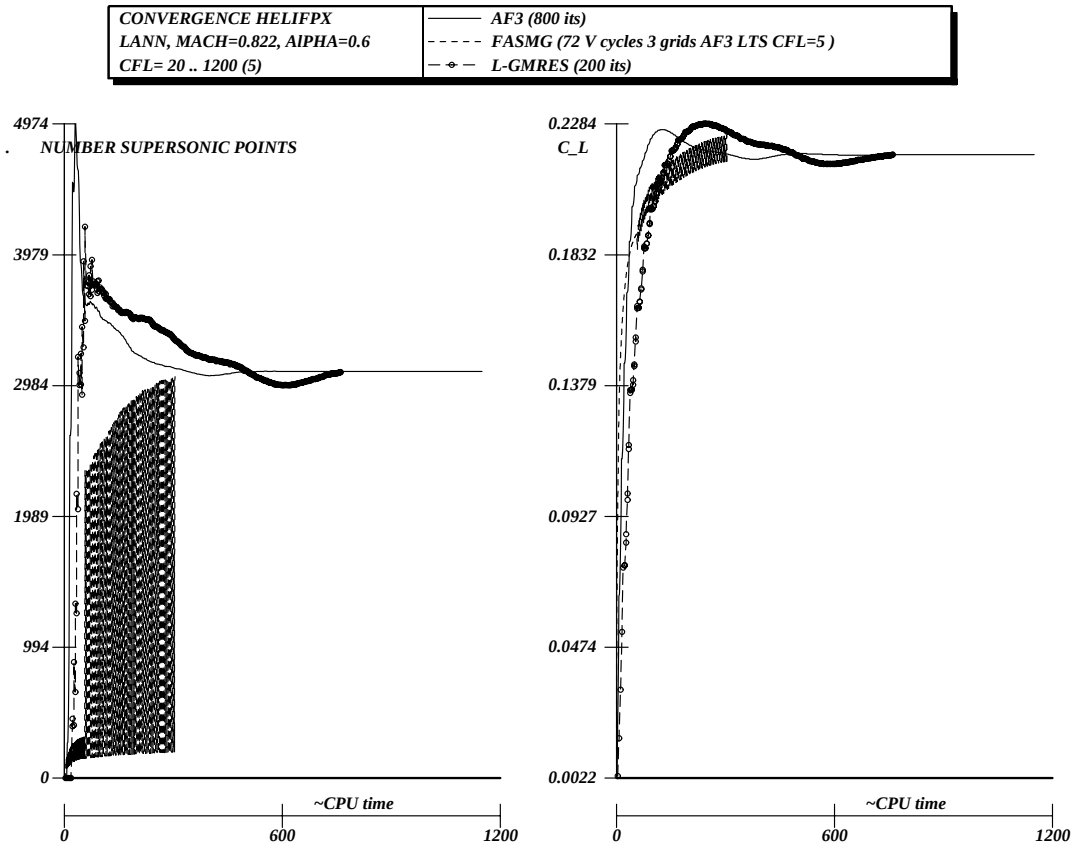

Fig. 6: Convergence characteristics for the LANN wing at Mach = 0.822, α = 0.6 degrees; LTS means local time stepping, L-GMRES means AF3 preconditioned GMRES

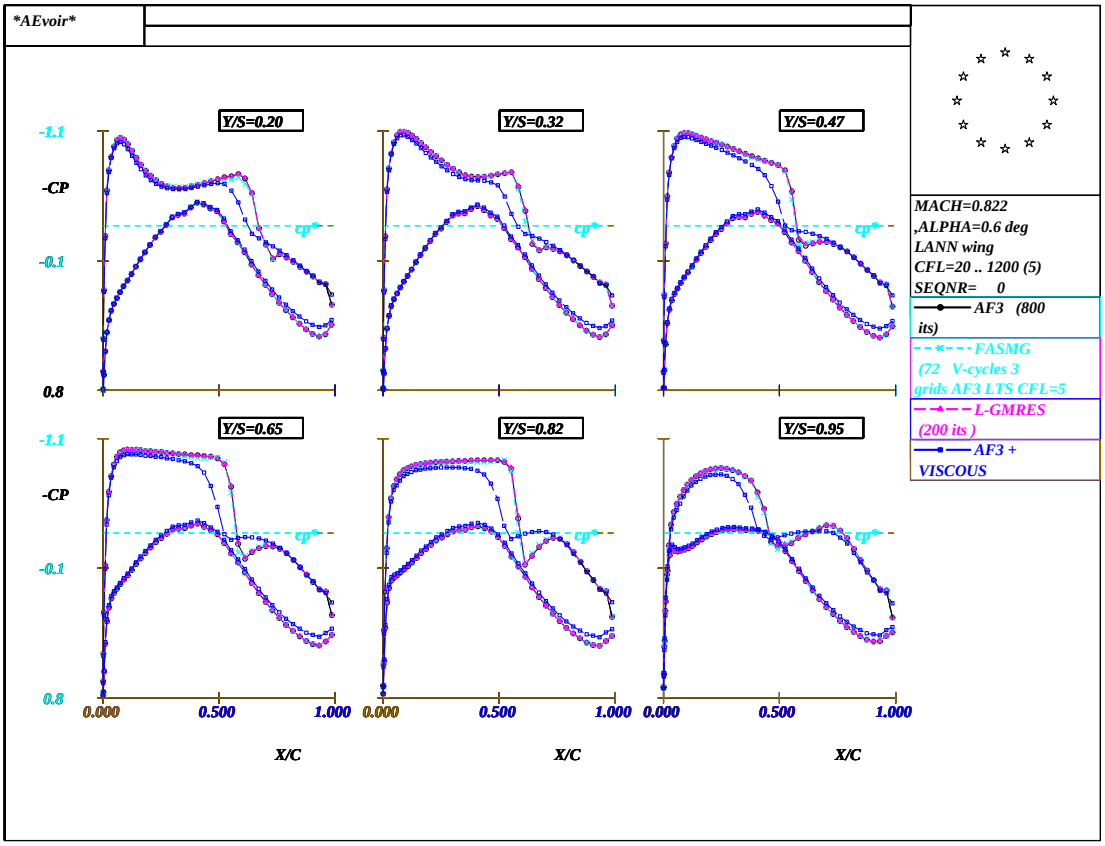

Fig. 7: Comparison of pressure coefficients at selected span stations for the LANN wing at Mach = 0.822, α = 0.6 degrees and Reynolds = 6.1 Million; LTS means local time stepping, L-GMRES means AF3 preconditioned GMRES

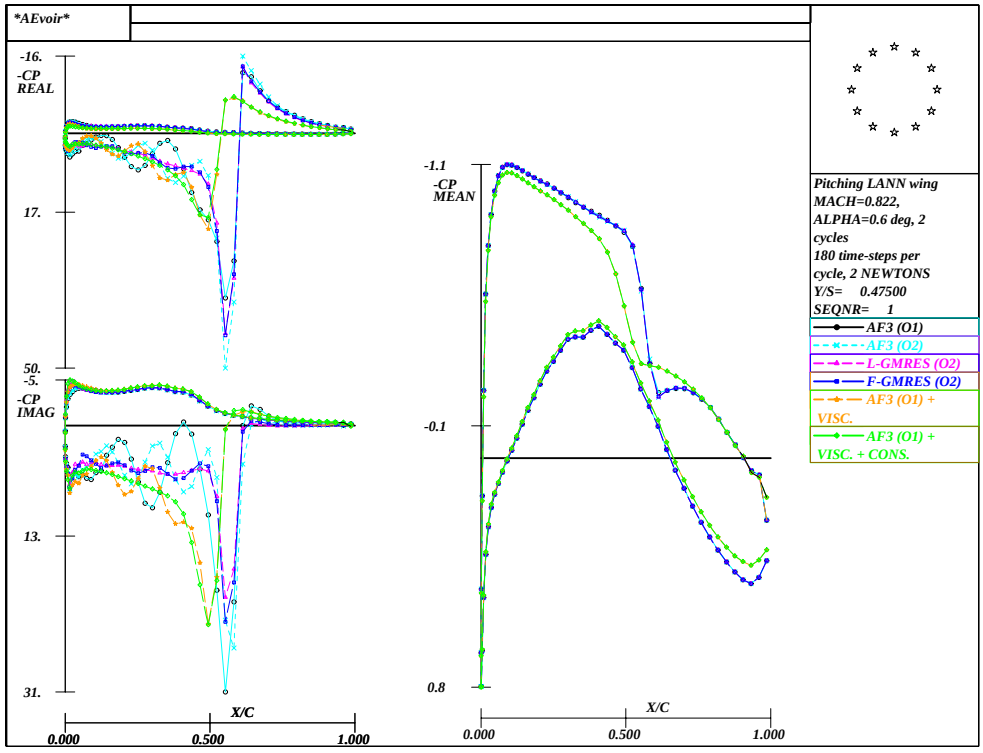

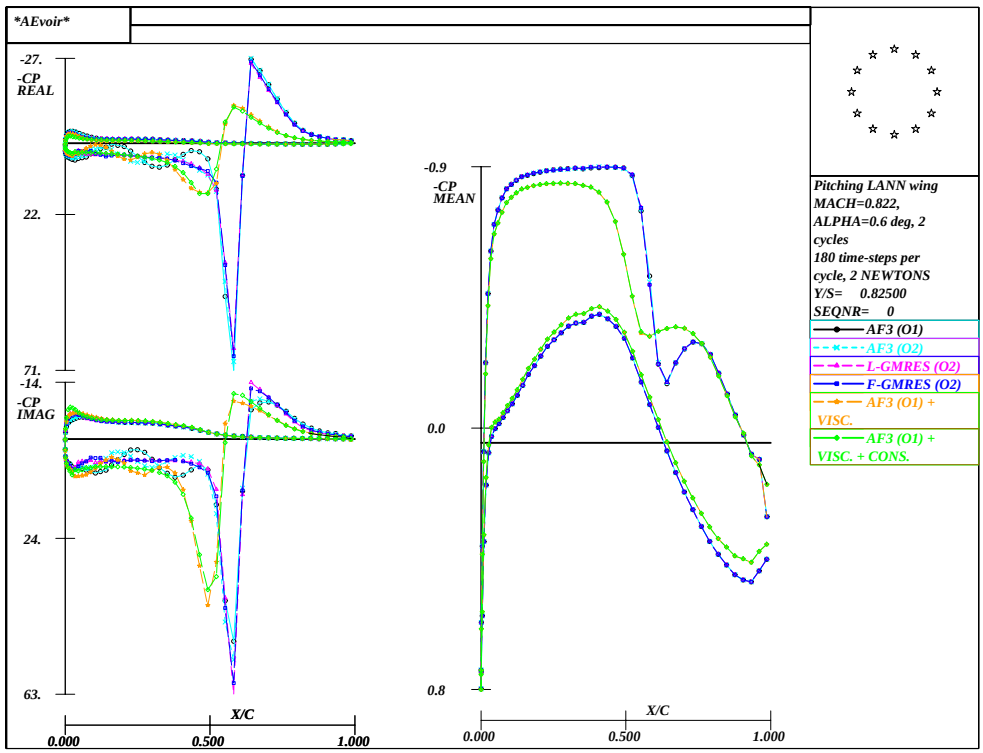

Fig. 8: Comparison of mean and first harmonic pressure coefficients at selected span stations for a pitching LANN wing at Mach = 0.822, α_{min} = 0.35 degrees, α_{max} = 0.85, k = 0.101 and Reynolds = 6.1 Million; L-GMRES means application of AF3 preconditioned GMRES, F-GMRES means application of matrix free GMRES, O1 and O2 mean first and second order temporal accuracy, respectively, CONS means time-consistent coupling with boundary layer

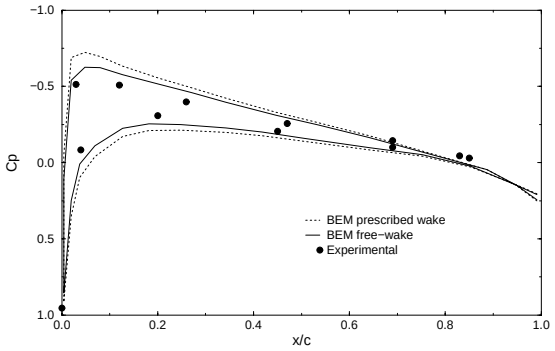

Section: $r/R = 0.50$

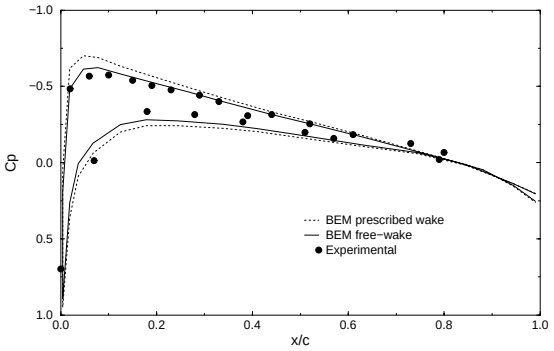

Section $r/R = 0.68$.

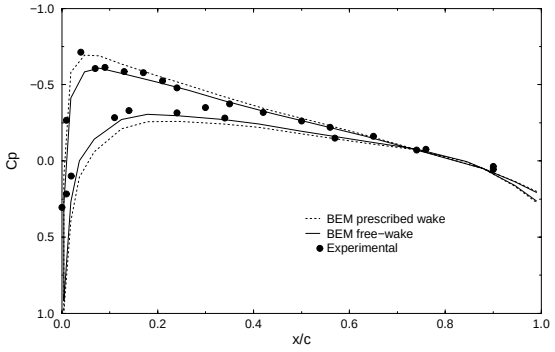

Section: $r/R = 0.80$

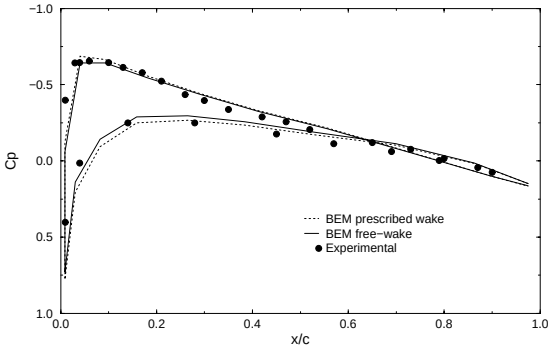

Section $r/R = 0.89$

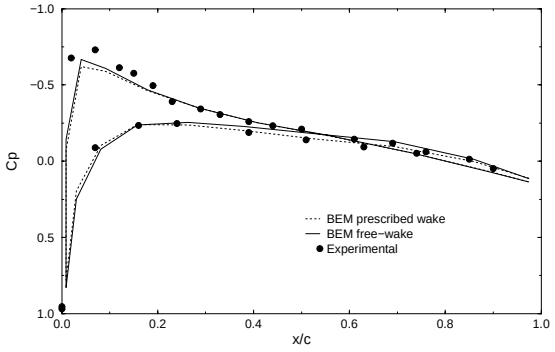

Section $r/R = 0.96$

Fig. 9: Comparison of pressure coefficients at selected span stations for the Caradonna-Tung rotor at $M_{\omega R} = 0.61$ and $\theta = 5$ degrees. (—— free-wake)

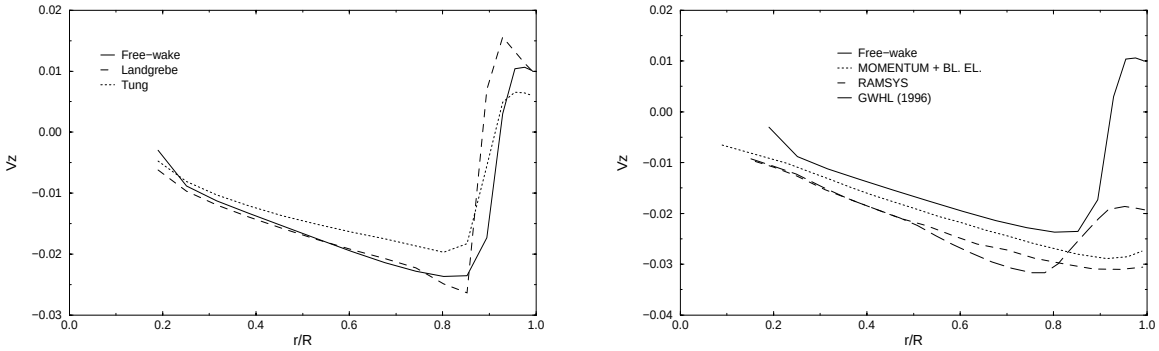

(a) (b)

Fig. 10: Comparison of the spanwise distribution of the inflow at $x/c = 0.25$ for the Caradonna-Tung rotor at $M_{\omega R} = 0.61$ and $\theta = 5$ degrees. (—— free-wake)

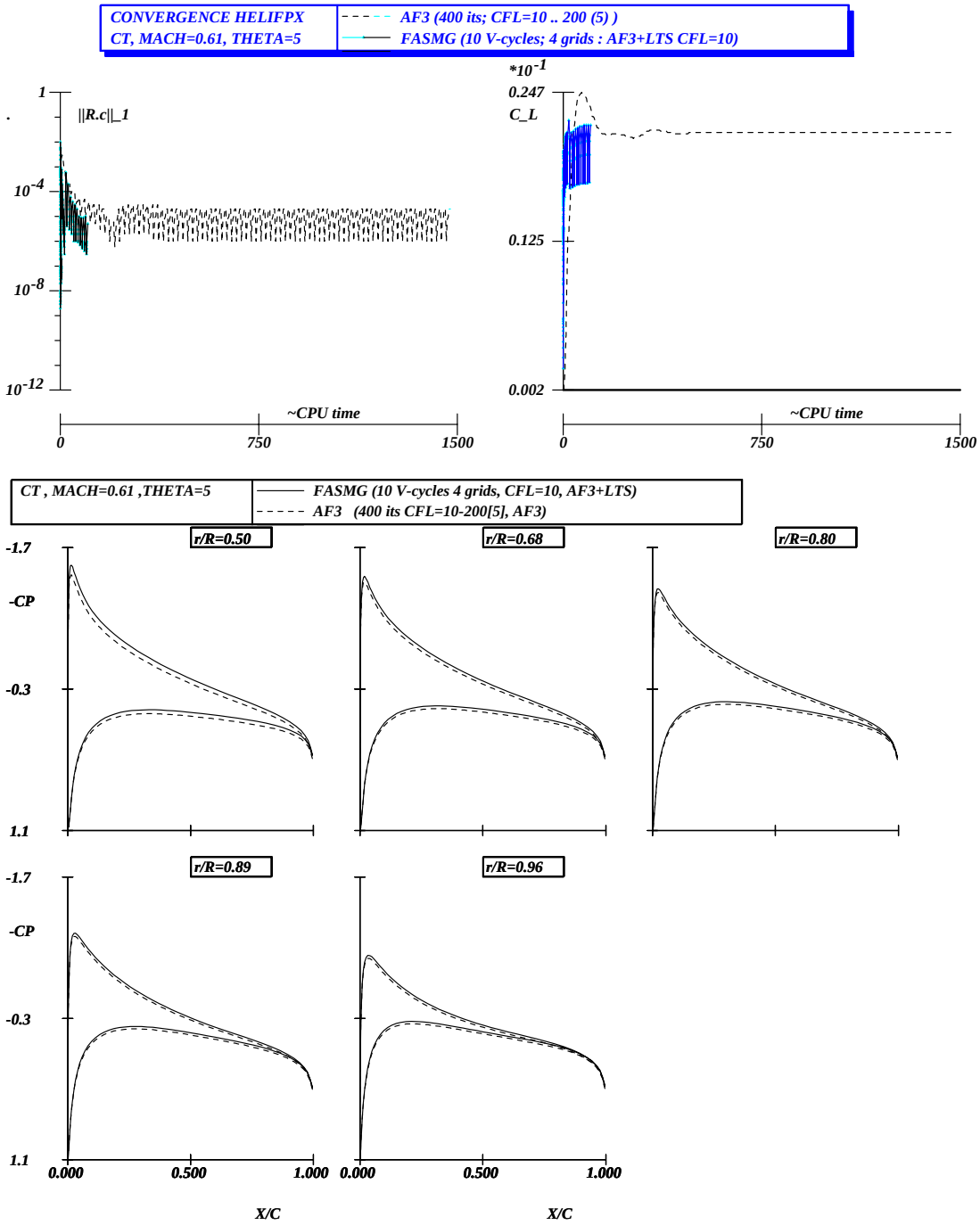

Fig. 11: Convergence characteristics and comparison of pressure coefficients for the Caradonna-Tung rotor at $M_{\omega R} = 0.61$ and $\theta = 5$ degrees; no induced wake model, no boundary layer; LTS means local time stepping

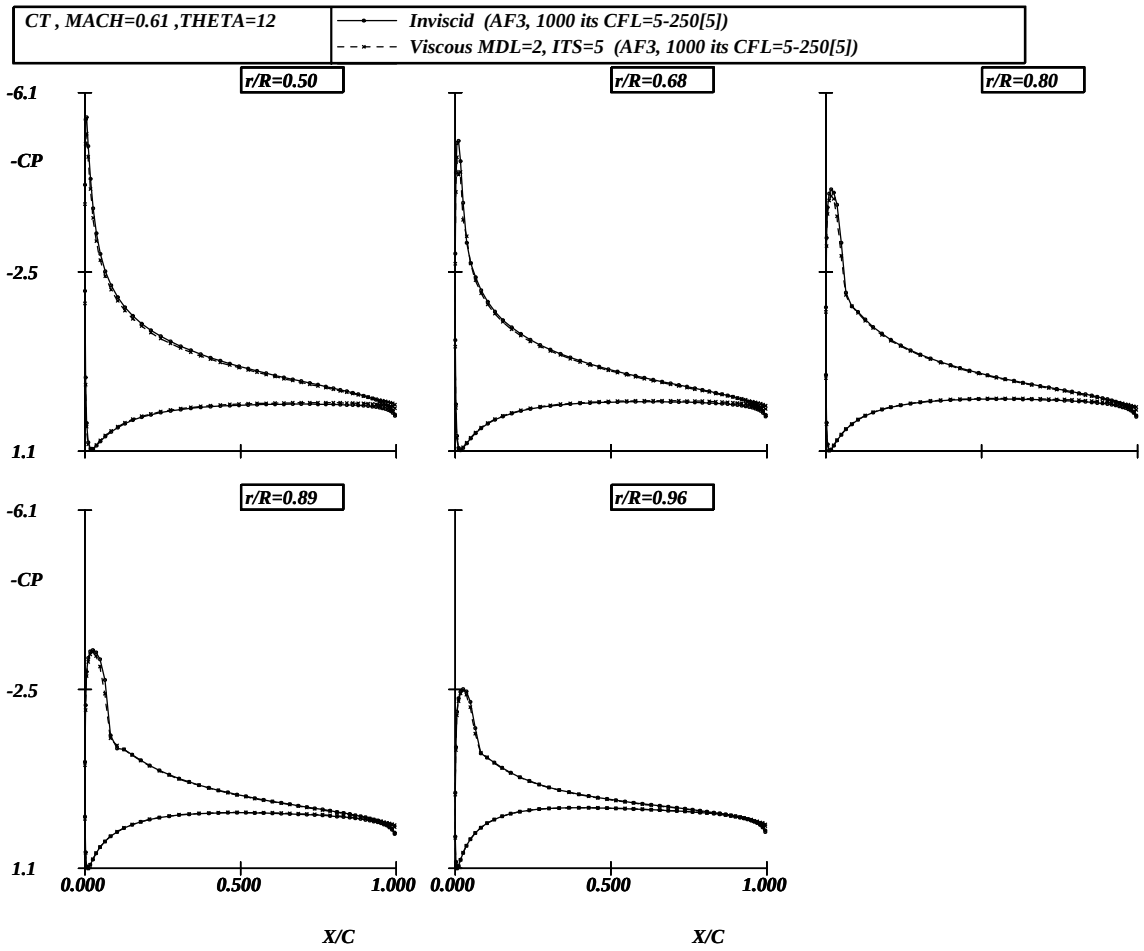

Fig. 12: Comparison of pressure coefficients at five selected span stations for the Caradonna-Tung rotor at $M_{\omega R} = 0.61$, $\theta = 12$ degrees and Reynolds = 7 Million; no wake inflow model, MDL means turbulence model, ITS means boundary layer update frequency

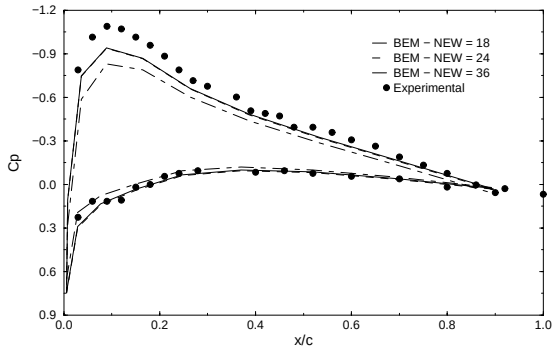

$(\Psi = 0^\circ — r/R = 0.75)$

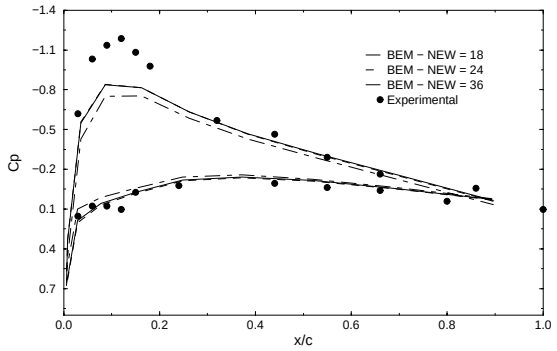

$(\Psi = 0^\circ — r/R = 0.87)$

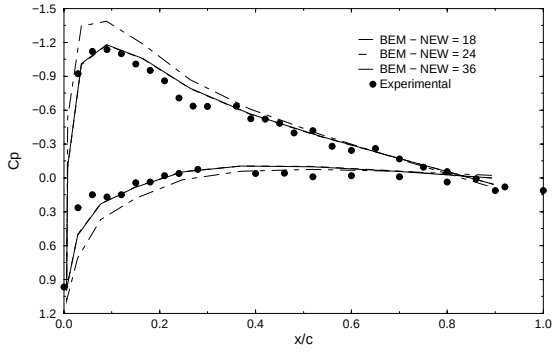

$(\Psi = 120^\circ — r/R = 0.75\ )$

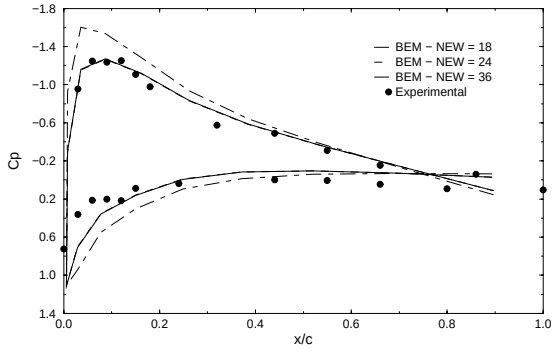

$(\Psi = 120^\circ — r/R = 0.87\ )$

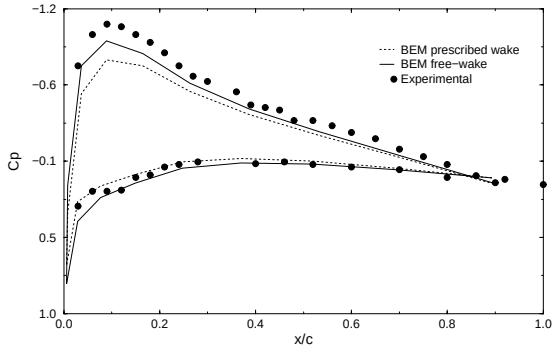

$(\Psi = 0^\circ — r/R = 0.75)$

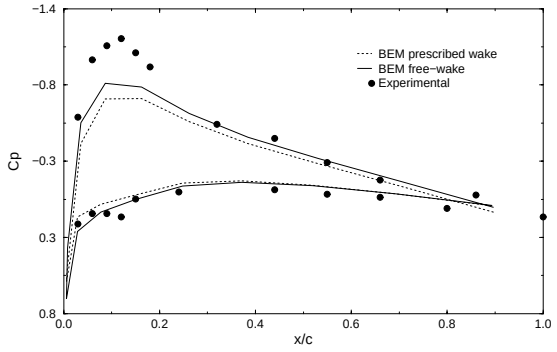

$(\Psi = 0^\circ — r/R = 0.87)$

Fig. 13: Pressure coefficient distribution at selected span and azimuthals for a four bladed BO-105 rotor in pitching motion

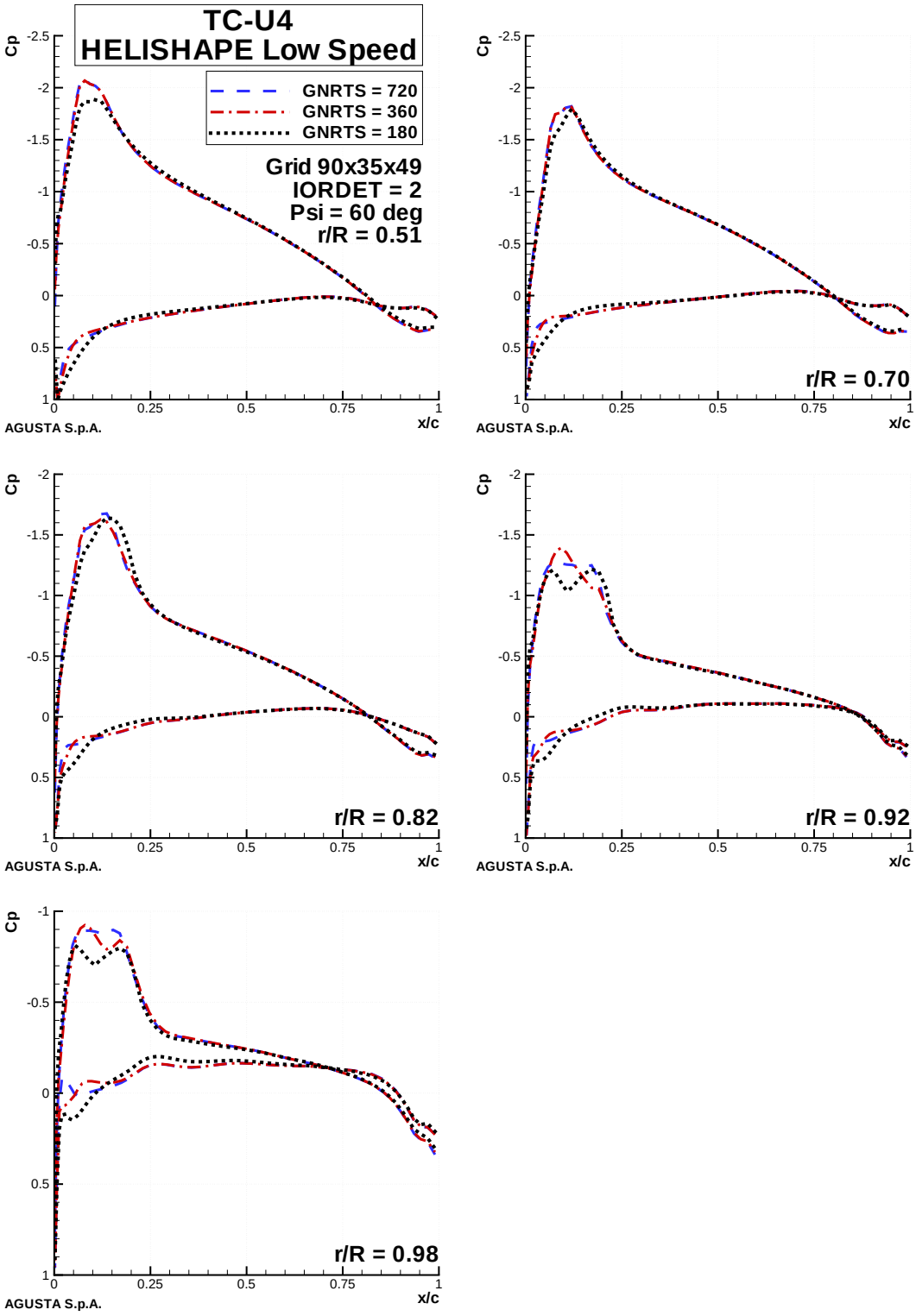

Fig. 14: Effect of time step ($\frac{2\pi}{GNRTS}$) on pressure coefficient predictions at five span stations for 7A rotor at $\Psi = 60$ degrees in low speed forward & level flight, Advance ratio $\mu = 0.167$, $C_T/\sigma = 0.0815$ and Rotational velocity $M_{\omega R} = 0.616$; AF3, second order temporal accurate & 2 subiterations

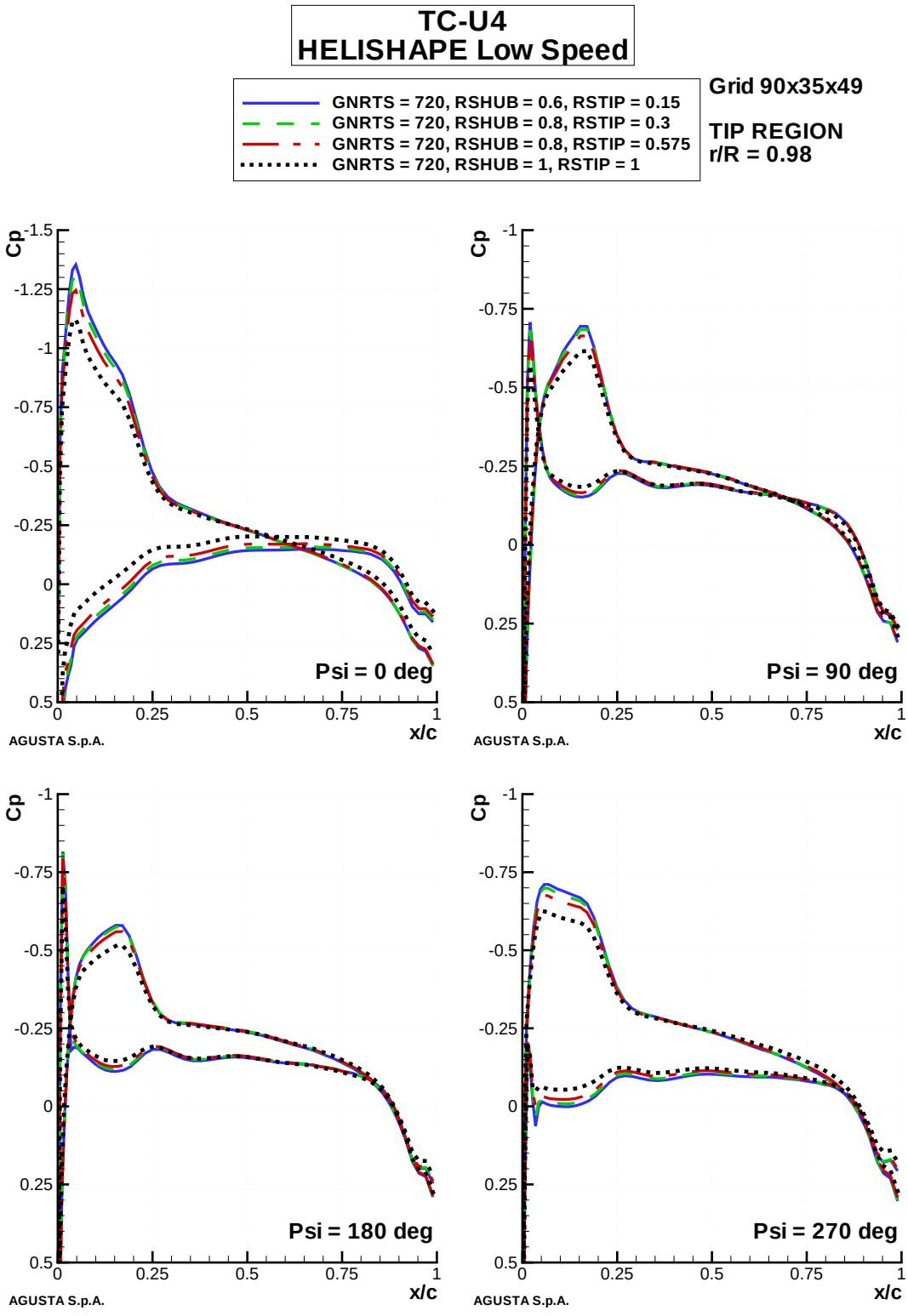

Fig. 15: Effect of spanwise grid distribution at tip (RSTIP) and hub (RSHUB) on pressure coefficient predictions for 7A rotor in low speed forward & level flight, Advance ratio $\mu = 0.167$, $C_T/\sigma = 0.0815$ and rotational velocity $M_{\omega R} = 0.616$; RSTIP $\approx$ grid spacing at tip, RSHUB $\approx$ grid spacing at hub

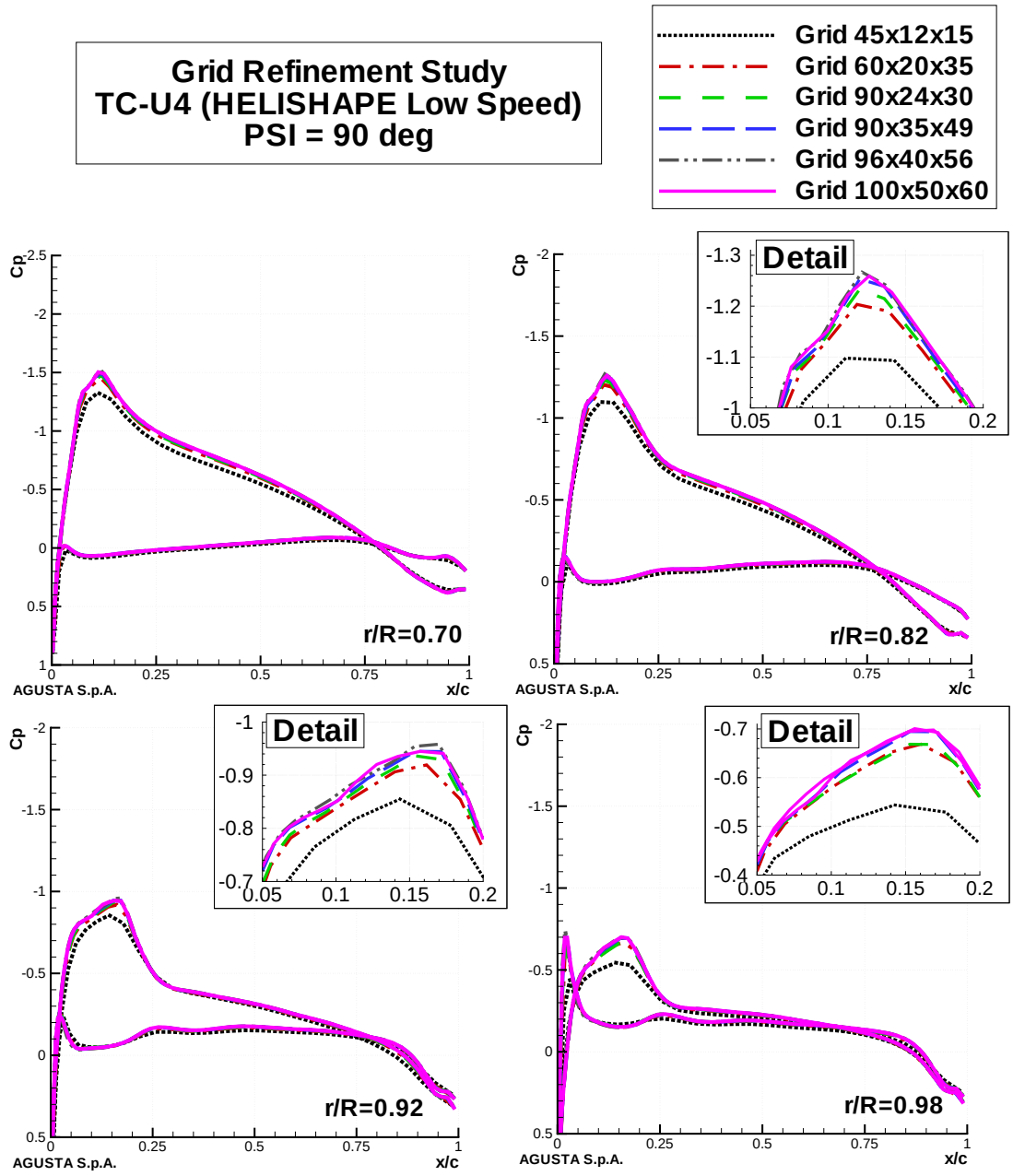

Fig. 16: Effect of grid distribution on pressure coefficient predictions at four span stations for 7A rotor in low speed forward & level flight, Advance ratio $\mu = 0.167$, $C_T/\sigma = 0.0815$ and rotational velocity $M_{\omega R} = 0.616$ ($\Psi = 90$ degrees). CH-grid dimensions given by triplets (chord, span and normal directions)

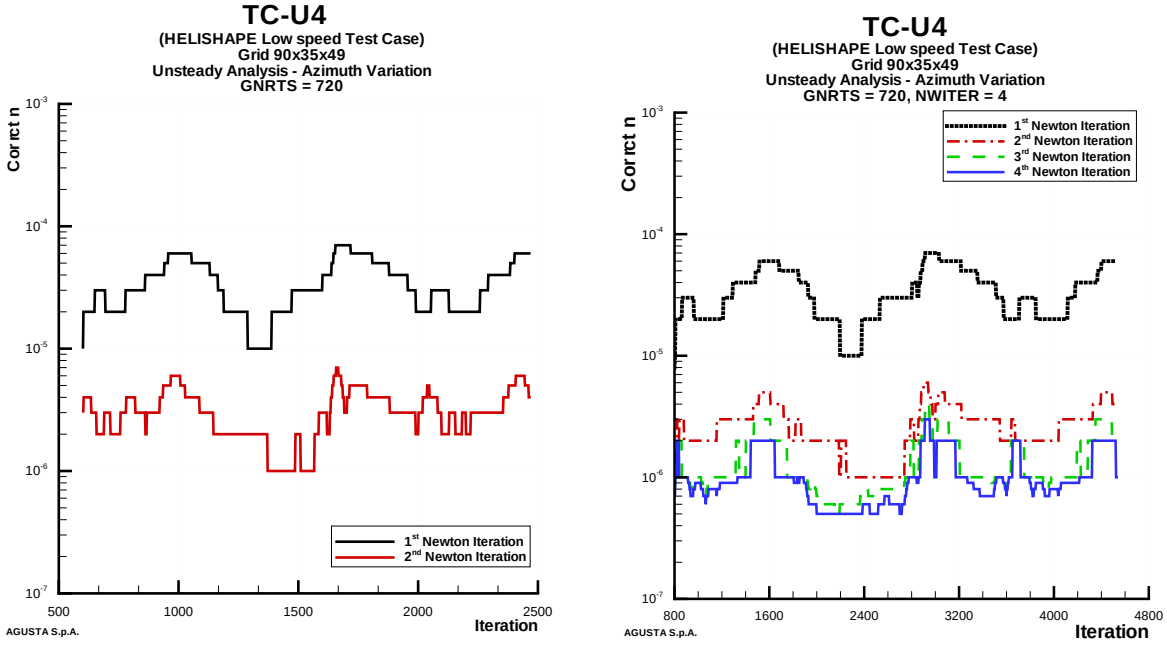

Fig. 17: Effect of subiterations (AF3) on correction (= $||c||_\infty$) for 7A rotor in low speed forward & level flight, Advance ratio $\mu = 0.167$, $C_T/\sigma = 0.0815$ and Rotational velocity $M_{\omega R} = 0.616$. ($\Psi = \frac{Iteration}{2\text{(left)},4\text{(right)}}$ degrees)

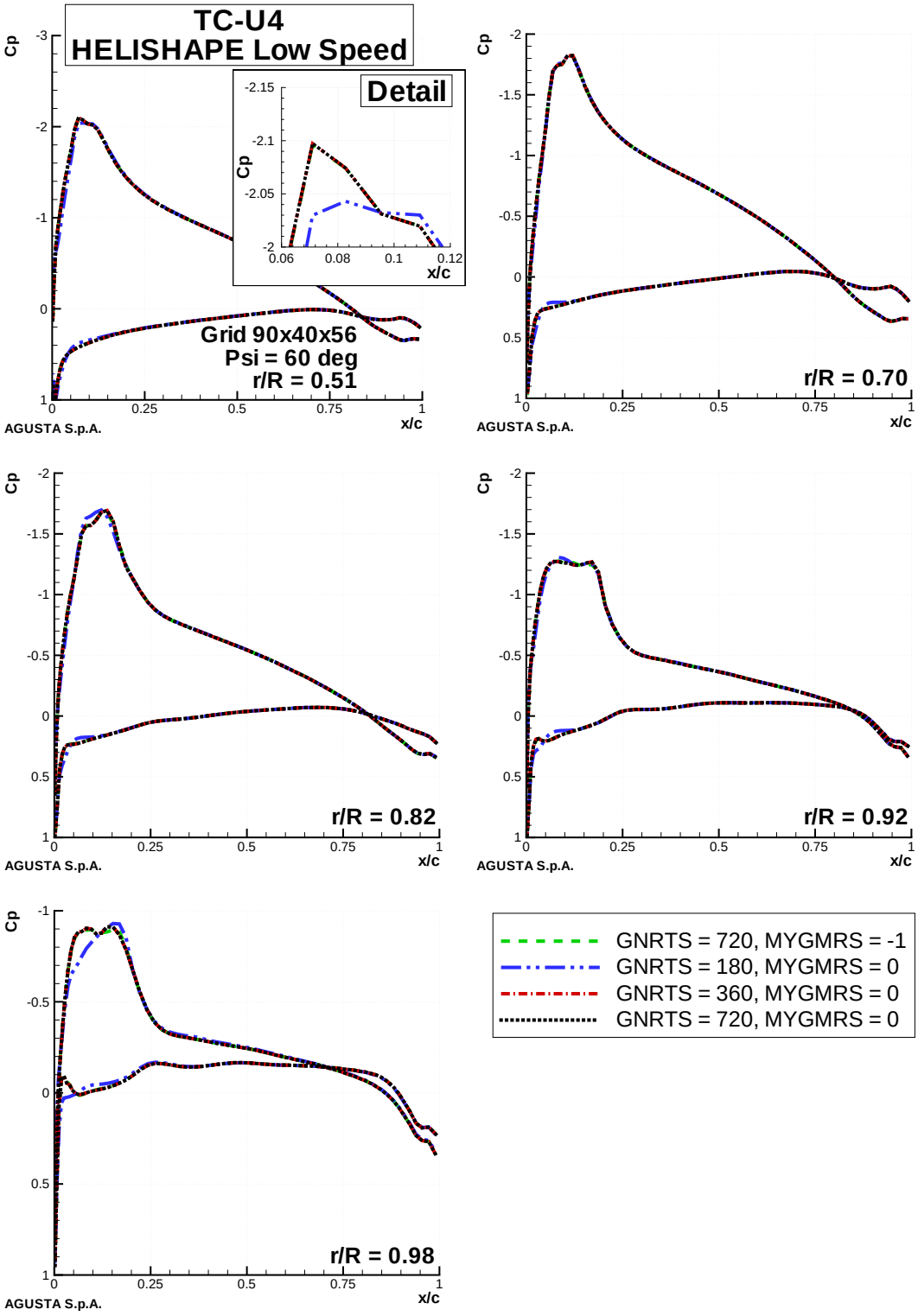

Fig. 18: Effect of time step ($\frac{2\pi}{GNRTS}$) and GMRES application (MYGMRS, 0= AF3 preconditioned, -1 AF3 only) on pressure coefficient predictions at five span stations for 7A rotor ($\Psi = 60$ degrees) in low speed forward & level flight, Advance ratio $\mu = 0.167$, $C_T/\sigma = 0.0815$ and Rotational velocity $M_{\omega R} = 0.616$; second order time accurate and & 2 subiterations

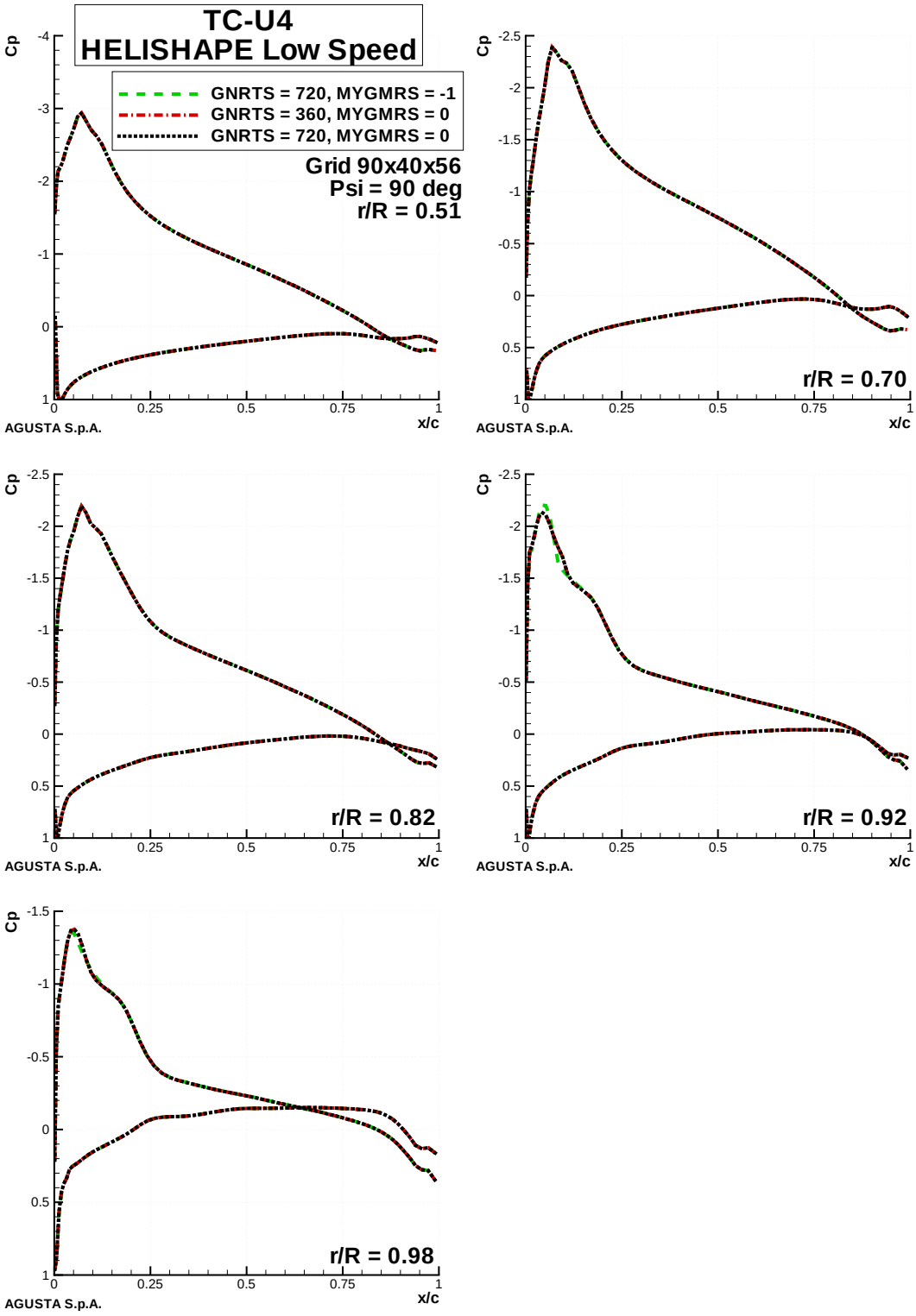

Fig. 19: Effect of time step ($\frac{2\pi}{GNRTS}$) and GMRES application (MYGMRS, 0= AF3 preconditioned, -1 AF3 only) on pressure coefficient predictions at five span stations for 7A rotor ($\Psi = 90$ degrees) in low speed forward & level flight, Advance ratio $\mu = 0.167$, $C_T/\sigma = 0.0815$ and Rotational velocity $M_{\omega R} = 0.616$; second order time accurate & 2 subiterations

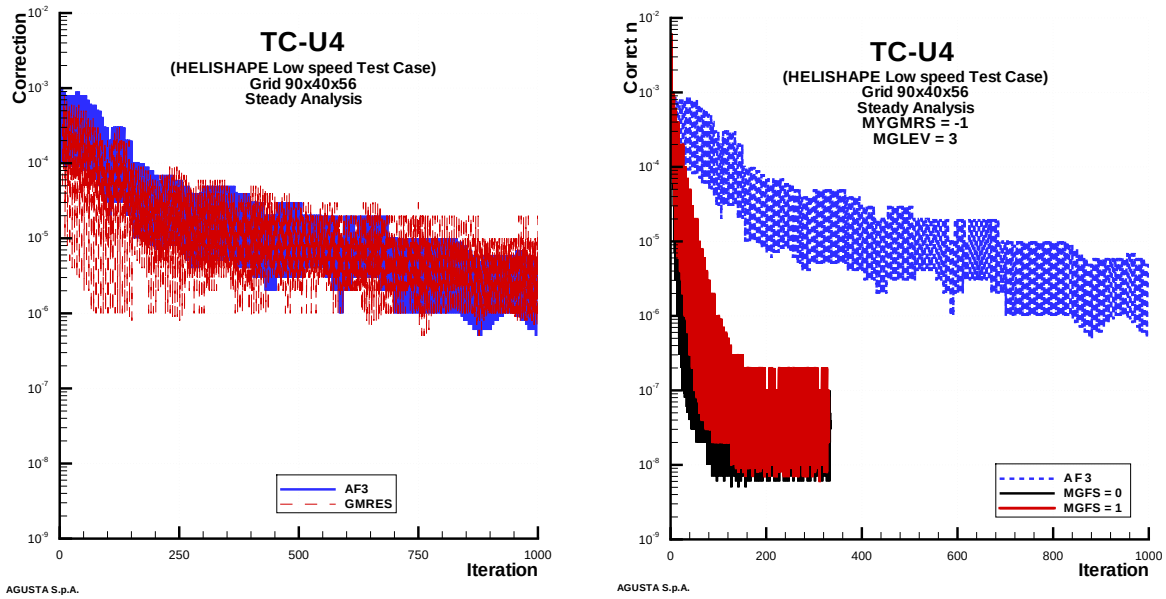

Fig. 20: Effect of GMRES (left), FAS-MG (right) (MGFS, 0 = FAS-MG, 1 = FAS-MG & full multi-grid) , AF3 (both) and variable time stepping (CFL = 10..100) on correction (= $||c||_\infty$) for 7A rotor at $M_{\omega R} = 0.616$

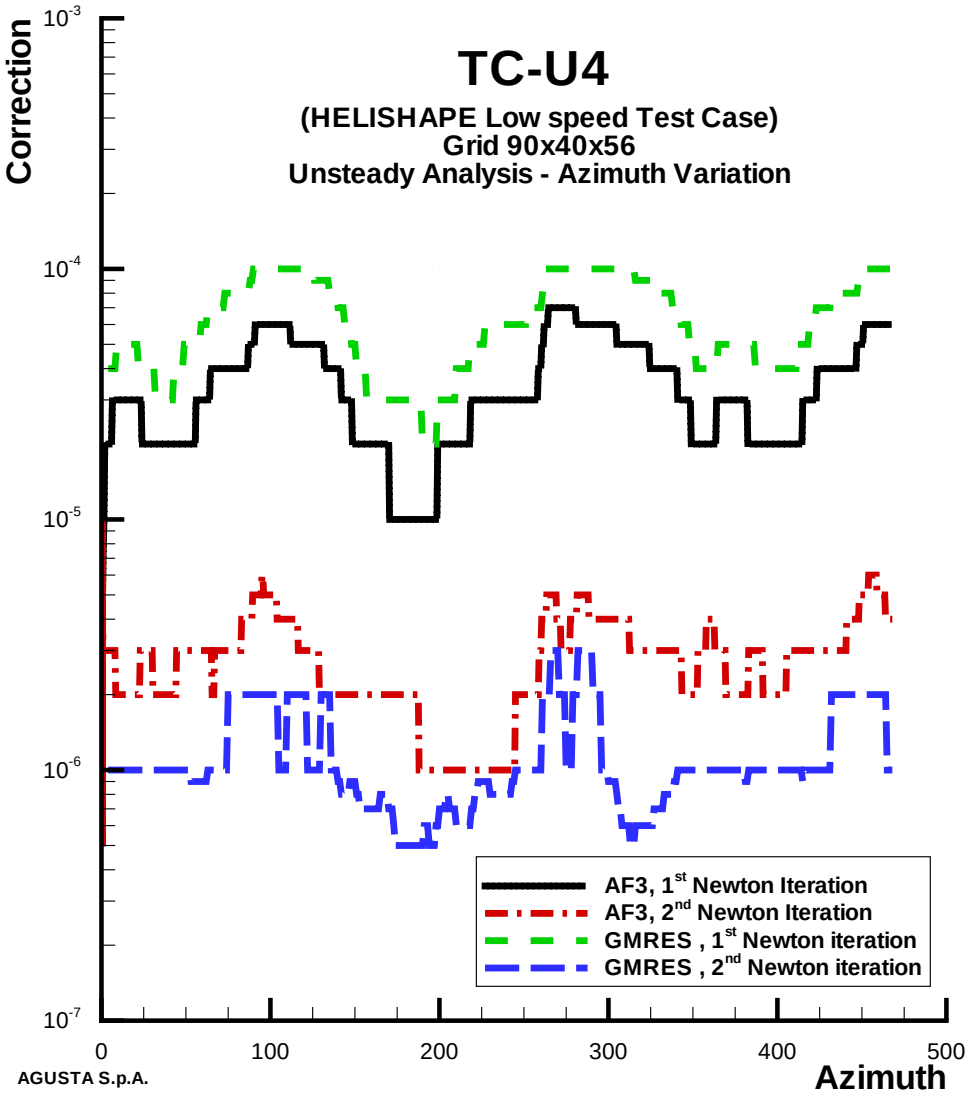

Fig. 21: Effect of GMRES and AF3 on correction (= $||c||_\infty$) for 7A rotor in low speed forward & level flight, Advance ratio $\mu = 0.167$, $C_T/\sigma = 0.0815$ and Rotational velocity $M_{\omega R} = 0.616$; second order time accurate & 2 subiterations